

# Comparative Analysis of the Characteristics of the Vortex Wake behind a Flapping Wing Performing Oscillations of Different Types

V. K. Vineeth<sup>a,\*</sup> and D. K. Patel<sup>a,\*\*</sup>

<sup>a</sup>*School of Mechanical Engineering, Vellore Institute of Technology, Vellore, Tamil Nadu, India-632014*

<sup>\*</sup>*e-mail: vineeth.vk1019@gmail.com*

<sup>\*\*</sup>*e-mail: devendra21082@gmail.com*

Received June 27, 2021; revised October 5, 2021; accepted November 1, 2021

**Abstract**—The wake characteristics of a custom-designed airfoil performing pitching oscillations, heaving oscillations, and a combination of pitch and heave oscillations are compared in this study. The influence of flapping parameters are investigated at a constant Reynolds number  $Re_c = 2640$  and is presented for the Strouhal numbers based on the oscillation amplitude,  $St_A$ , varying in the  $0.1 \leq St_A \leq 0.4$  range. The generation of vorticity above and below the airfoil depends on the airfoil's initial direction of motion and remains the same for all types of flapping oscillations investigated. The evolution of the leading-edge and trailing-edge vortices is presented. The heaving oscillations of the airfoil are found to have a greater influence on the characteristics of the leading edge vortex. The wake behind the combined pitch-heave oscillations appears to be governed by pitching oscillations below  $St_A = 0.24$ , whereas it is driven by heaving oscillations above  $St_A = 0.24$ . The force computations indicate that the mere existence of the reverse von Kármán street is not sufficient to develop the thrust on the airfoil. The periodic component of velocity fluctuations significantly influences the wake characteristics. The anisotropic stress field developed around the airfoil due to the periodic fluctuations of the velocity is presented. The coherent structures developed in the wake are identified using the proper orthogonal decomposition and a qualitative comparison of the structures for different flapping oscillations is presented. The energy transfer from the flapping airfoil to the fluid for different flapping oscillations is highest for heaving oscillations followed by combined pitch-heave oscillations and pitching oscillations.

**Keywords:** flapping airfoil, pitching motion, heaving motion, laminar flow, coherent structures, force coefficients

**DOI:** 10.1134/S0015462822020124

The flapping mechanisms used by insects, birds, and fishes are extremely capable of achieving highly efficient locomotion. The development of unmanned aerial vehicles and micro/nano air vehicles requires sophisticated and efficient flapping mechanisms. The flapping airfoil dynamics has generated a great deal of interest recently because of this capability. The widely considered flapping mechanisms include pitching oscillations, heaving oscillations, and combined pitch-heave oscillations. A considerable number of studies explored pitching oscillations [1–4], heaving oscillations [3–8], and combined pitch-heave oscillations [9–12]. The vortices behind the oscillating airfoil form different arrangements in the wake, such as von Kármán type, reverse von Kármán type, deflected type, and completely irregular arrangement. Triantafyllou et al. [13] observed the existence of the reverse von Kármán street behind a pitching-heaving airfoil in the Strouhal number (flapping parameters expressed in the dimensionless form) range of 0.25–0.35 and the existence of the von Kármán street below this range. Lai and Platzer [5] showed that the transition between flow patterns in the wake of a plunging airfoil occurs in the dimensionless plunge velocity (equivalent of Strouhal number) range 0.2–0.4. The deflected type wake arrangement behind a heaving airfoil was visualized by Jones et al. [14] and the similar arrangement behind a pitching-heaving airfoil was elucidated by Vandenberghe et al. [15]. Schnipper et al. [16] showed that the transitions behind the pitching airfoil appear in the Strouhal number range of 0.1–0.3.

Jones and Platzer [17] pointed out that the von Kármán type arrangement characterizes a drag producing wake, while the reverse von Kármán type arrangement characterizes a propulsive wake. The symmetry

breaking of the reverse von Kármán wake and generation of the deflected wake were found to develop both thrust and lift. Godoy-Diana et al. [18] identified transitions in the wake of the pitching airfoil and visualized the von Kármán wake, the reverse von Kármán wake, and the deflected wake. Badrinath et al. [19] presented transitions behind the heaving airfoil and Bose and Sarkar [20] reported transitions behind an airfoil performing combined pitch and heave. In the deflected wake, vortices of opposite sign form dipoles and propagate towards the far wake. The dipole formation behind the pitching airfoil and the plunging airfoil were reported by Godoy-Diana et al. [21] and Cleaver et al. [22]. However, all these studies were performed for different airfoil profiles with different flapping parameters at different Reynolds numbers. Hence a comparison of the wake transitions for the same airfoil operating in the same parameter range for different types of flapping oscillations will be helpful to understand the flow field aerodynamics.

The literature also indicates the presence of multiple vortex wakes and their influence on the aerodynamic performance of flapping airfoils [23, 24]. Anderson et al. [24] observed the drag–thrust transition in the multiple vortex wake, in contrast to the wake with reverse von Kármán arrangement. Different researchers provided force measurements in the wake behind the pitching airfoil [25], the heaving airfoil [8], and the airfoil in combined pitch-heave [10, 26]. Force measurements by Anderson et al. [26] showed that the optimal thrust production by a pitching-heaving airfoil is observed in the Strouhal number range 0.25–0.40. Nevertheless, the force measurements were performed at different operational Reynolds numbers, and hence a direct comparison is not feasible. A comparison of different types of flapping oscillations at the same operational Reynolds number will be advantageous in the design and development of micro air vehicles. Most of these vehicles are designed to operate at Reynolds numbers ranging from  $10^3$  to  $10^4$  [27]. Correspondingly, a Reynolds number of 2640 is chosen for the present analysis. The literature highlighted an optimal performance of the airfoil in the Strouhal number range from 0.1 to 0.4, which is considered in the present study. The periodic oscillations are only investigated, as it is the most common form of the biological locomotion.

## 1. COMPUTATIONAL METHODOLOGY

### 1.1. Geometry and Kinematics of Airfoil

A symmetric airfoil with a semicircular leading edge and a wedge-shaped trailing edge is considered in this study. The ratio of the rigid airfoil thickness to the chord length  $D/C = 1/6$ . The pitching, heaving, and combined pitch-heave oscillations performed by the airfoil are presented in Fig. 1. The pitching motion executed by the airfoil is governed by the equation

$$\theta(t) = \theta_0 \sin 2\pi f t, \quad (1.1)$$

where  $\theta(t)$  is the instantaneous pitch amplitude and  $\theta_0$  is the maximum pitch amplitude;  $f$  is the flapping frequency, and  $t$  is time. The heaving motion executed by the airfoil is governed by the equation

$$h(t) = A \sin 2\pi f t, \quad (1.2)$$

where  $h(t)$  is the instantaneous heave amplitude and  $A$  is the maximum heave amplitude. Equations (1.1) and (1.2), taken together, govern the combined pitch-heave motion. No phase offset between the pitch and heave motion is considered in the present investigation. The combined pitch-heave motion is also addressed as combined motion in the manuscript. The flapping frequency and amplitude are presented in the dimensionless form, which is called the Strouhal number  $St_A$  based on the amplitude

$$St_A = \frac{2Af}{U}. \quad (1.3)$$

The airfoil performs the flapping motion in a uniform flow having a velocity  $U$  aligned with the coordinate  $x$ . The Reynolds number  $Re_c$  is based on the airfoil chord  $C$ , the flow velocity  $U$ , and the kinematic viscosity of the fluid  $\nu$

$$Re_c = \frac{UC}{\nu}. \quad (1.4)$$

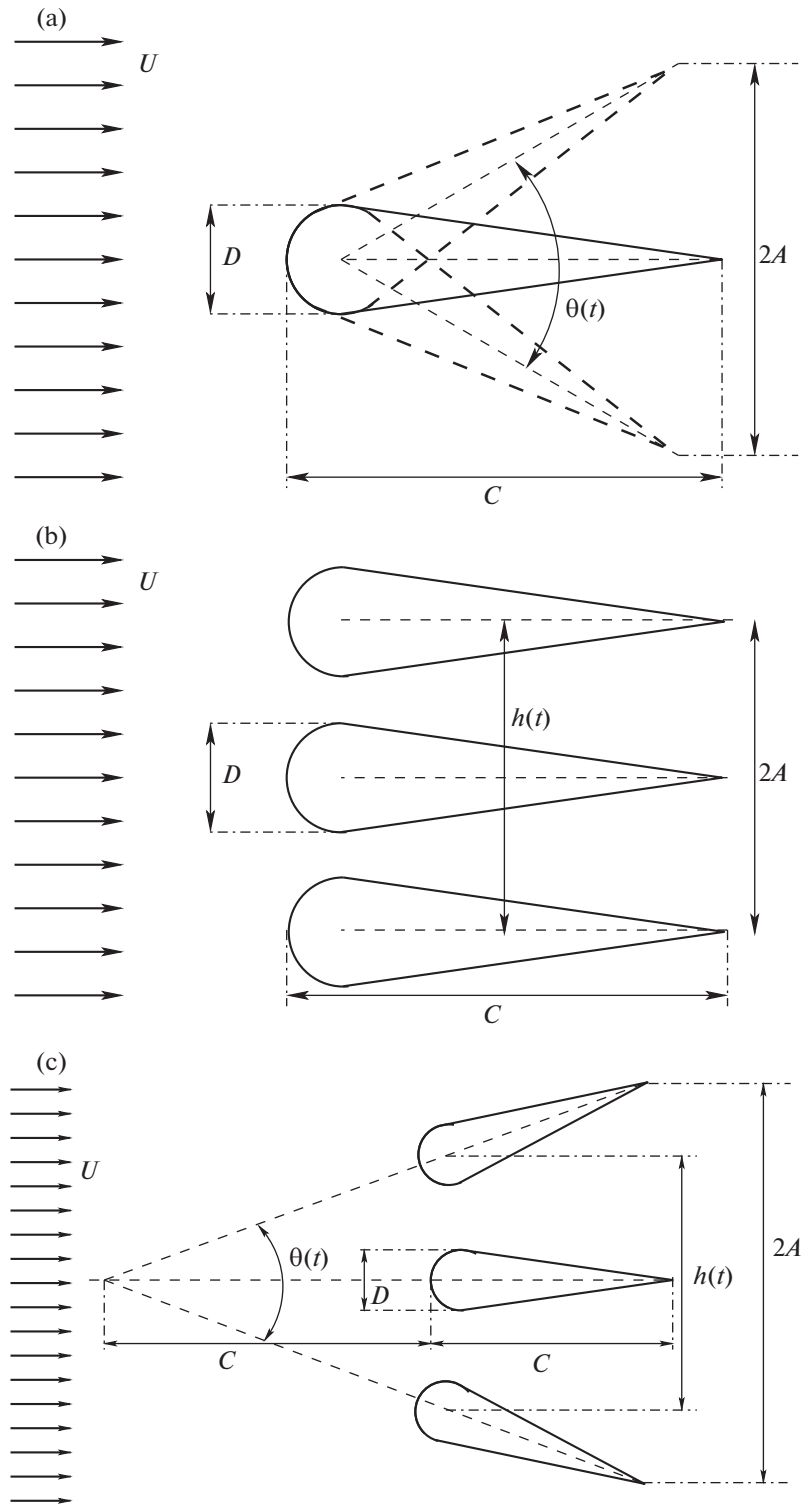


**Fig. 1.** Schematic diagram depicting the airfoil geometry and flapping kinematics (pitching (a), heaving (b), and combined pitch and heave (c)).

*1.2. Numerical Procedure*

The arbitrary Lagrangian–Eulerian (ALE) [28] approach is used to investigate the two-dimensional, unsteady, incompressible, laminar flow past a flapping airfoil. The Navier–Stokes equations are modified to employ the ALE method

$$\nabla \cdot \vec{u} = 0, \tag{1.5}$$

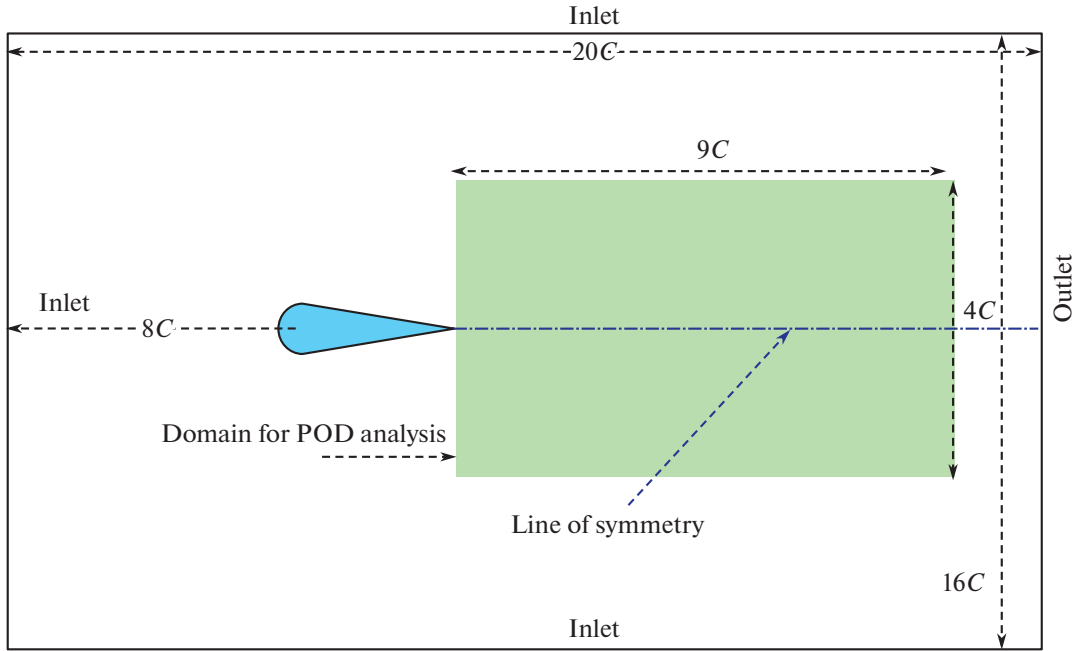


Fig. 2. Schematic representation of the computational domain.

$$\frac{\partial \bar{u}}{\partial t} + [(\bar{u} - \bar{u}_m) \cdot \nabla] \bar{u} = -\frac{\nabla p}{\rho} + \nu \nabla^2 \bar{u}. \quad (1.6)$$

Here,  $p$  is the pressure in the flow field,  $\bar{u}$  is the flow velocity, and  $\bar{u}_m$  is the grid point velocity. The fluid density  $\rho$  is constant over space and time. The time discretization is achieved using a second-order accurate implicit Euler scheme and the time step is adjusted so that the maximum Courant number is always less than 0.5. The advective and diffusive terms of the governing equations are discretized using the second-order upwind scheme and the second-order central difference scheme. The pressure-velocity coupling is achieved using the PIMPLE algorithm with three corrector loops. The present simulation employs one inner corrector loop and two outer corrector loops. The GAMG (generalized geometric-algebraic multi-grid) solver is used to solve the pressure correction equation. The solver selection is advantageous, as it removes any need for preconditioning. In each time step, the convergence criteria for the pressure and velocity are set to  $10^{-6}$ . The open-source computational fluid dynamics (CFD) package OpenFOAM [29] is used to simulate the flapping airfoil in the present investigation.

### 1.3. Boundary Conditions

The computational domain used in the present numerical investigation is shown in Fig. 2. The size of the computational domain is sufficiently large, so that the boundary effects on the solution are negligible. The left, top, and bottom boundaries of the computational domain are located at a distance of  $8C$  from the airfoil. The back boundary is considered at a distance of  $12C$  from the airfoil. The left, top, and bottom boundaries of the computational domain operate as an inlet, while the right side serves as an outlet. The inlet is provided with zero pressure gradient and a constant inlet velocity. Zero velocity gradient condition and the atmospheric pressure are provided at the outlet. The airfoil is considered as a moving wall and the no-slip conditions are imposed on the airfoil surface. The computational grid shown in Fig. 3 is more refined near the airfoil to capture the boundary layer phenomena. The grid is refined at different levels so that a maximum grid volume is obtained at the far boundary and a minimum grid volume is obtained close to the airfoil. The minimum grid volume close to the airfoil is  $1.5 \times 10^{-13}$  and the far boundary has a maximum grid volume of  $4.1 \times 10^{-9}$ . The maximum non-orthogonality of the grid is 50.43 with an average of 3.17 throughout the domain. The maximum skewness of the grid is limited to 0.71. A rectangular region of dimensions  $9C \times 4C$  is chosen inside the computational domain to perform the proper orthogonal decomposition analysis.

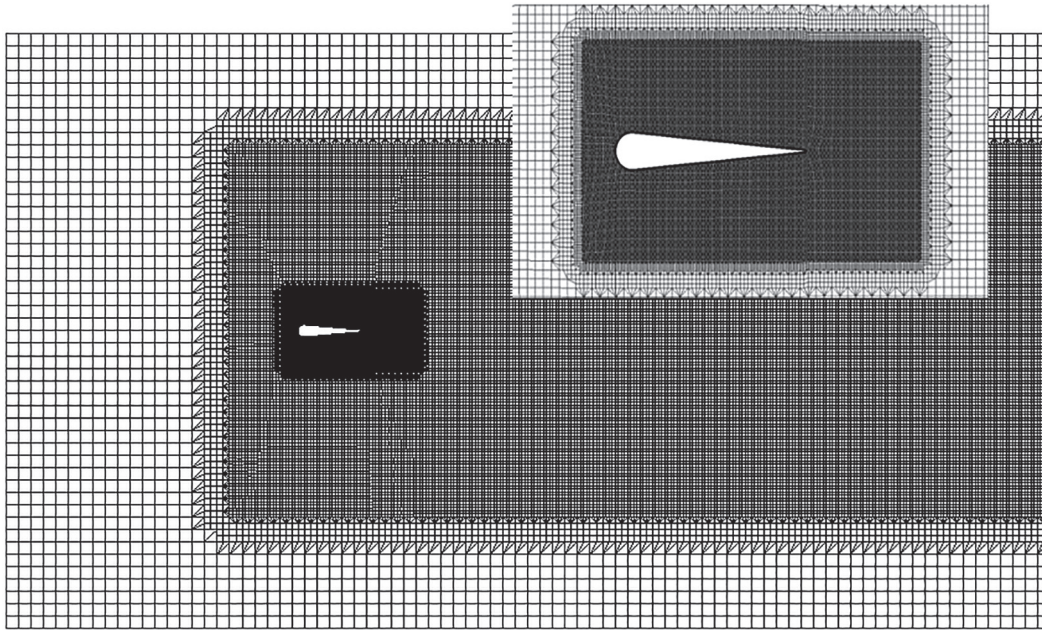
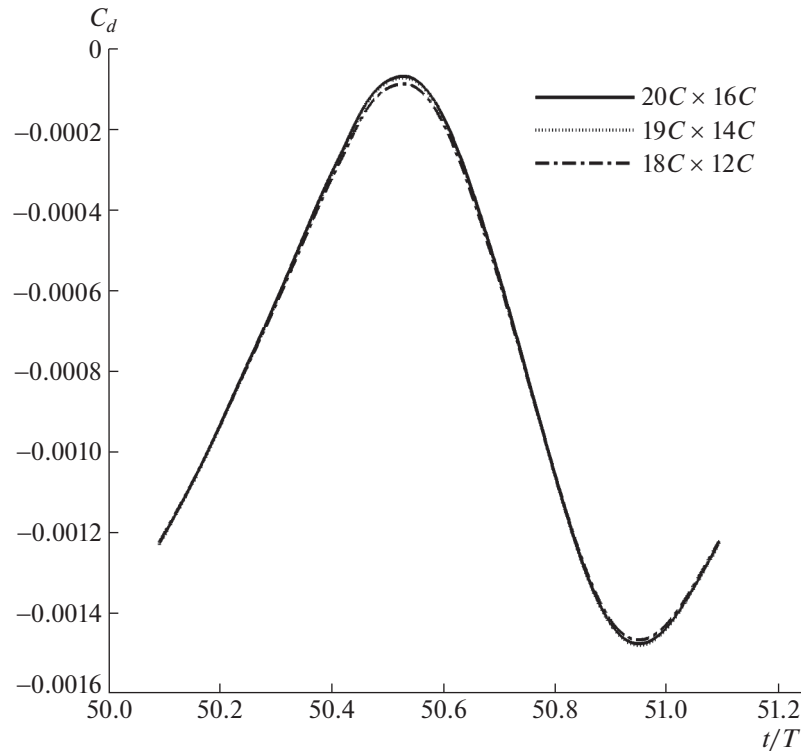


Fig. 3. The computational grid used in the present investigation; the mesh near the airfoil is provided in the inset.

#### 1.4. Solver Validation

The computational domain size is selected basing on the works of Zheng and Wei [30, 31], where the case of a two-dimensional flapping airfoil was studied. A domain-independent study is performed for an airfoil undergoing combined motion to analyze the influence of the computational domain. The domain sizes are varied both in the streamwise and transverse directions. The distance from the airfoil to the outlet and the distance to the top and bottom boundaries are increased by an order of one chord length. The distance from the airfoil to the inlet is kept fixed. The variation of the drag coefficient appears to be similar for the domain sizes  $20C \times 16C$  and  $19C \times 14C$  (Fig. 4). A grid independence test was performed on the airfoil undergoing the combined pitch-heave motion to ensure that the effect of grid size on the solution is redundant. The number of gridpoints in the domain is increased to obtain four different grid densities, and the variation of the drag coefficient  $C_d$  and the lift coefficient  $C_l$  for each grid density was computed for one complete cycle. The different grid densities were obtained by reducing the grid size close to the airfoil. Figures 5a and 5b present the variations in the drag ( $C_d$ ) and lift ( $C_l$ ) coefficients experienced by the airfoil for different grid densities. A grid distribution with  $3.2 \times 10^5$  cells in the domain was found sufficient to capture the flow dynamics close to the airfoil. The variation in mean flow velocity  $U_{\text{mean}}$  was computed to assess the grid independence in the wake region. The variation in  $U_{\text{mean}}$  along the line of symmetry and perpendicular to it is shown in Fig. 6. Along the line of symmetry the variation is considered up to a distance of  $8C$  (Fig. 6a), while the variation perpendicular to the line of symmetry is plotted at a distance of  $8C$  from the trailing edge of the airfoil (Fig. 6b). The  $U_{\text{mean}}$  variation is almost the same for successive grid distributions with  $3.2 \times 10^5$  cells and  $1.78 \times 10^5$  cells in the domain. A grid density of  $3.20 \times 10^5$  is chosen to ensure the grid independence of the numerical solution.

The wake structure obtained using the present solver is compared with previous experimental results available in the literature. The pure pitching and pure heaving motions are qualitatively validated. The flow visualization made by Koochesfahani [32] in the wake of a pitching airfoil is compared with the vorticity patterns obtained using the present solver. Koochesfahani [32] presented a neutral wake (Fig. 7a) at a reduced frequency  $k = 6.7$  and a multiple vortex wake (Fig. 7c) at  $k = 3.1$ . The wake patterns obtained numerically (Figs. 7b and 7d) appear to be in close agreement with the observed experimental patterns. The dye flow visualization results reported by Jones et al. [14] for a heaving airfoil are compared with the wake vorticity contours obtained using the present solver in Fig. 8. For a reduced frequency  $k = 3$  Jones et al. [14] reported a thrust wake (Fig. 8a) and a deflected wake (Fig. 8c) at a higher value of  $k = 12.5$ .



**Fig. 4.** Variation in the drag coefficient for three different domain sizes.

The thrust wake and the deflected wake obtained from the present computations (Figs. 8b and 8d) are in close agreement.

Quantitative validation of the solver is presented in Fig. 9. The variation of time-averaged thrust coefficient ( $\overline{C}_t$ ) with the dimensionless flapping frequency ( $f^* = \frac{f \times C}{U}$ ) obtained in the present simulation is compared with the experimental measurements of Buren et al. [33] and Bose et al. [34]. The range of flapping frequency considered and the Reynolds number, at which the investigations are performed in the present study, are different from the reported results. For this reason, the comparison is made providing different axis scales for the experimental and computational investigations. The experimental data are plotted with the left and bottom axes as the coordinate axes, while the computational data are plotted with the right and top axes as the coordinate axes. The coefficient of thrust from the experimental measurements and the computed data exhibit the same trend with increase in the flapping frequency.

## 2. RESULTS AND DISCUSSION

The laminar incompressible flow behind a flapping airfoil is analyzed numerically. The pitching, heaving, and combined pitch-heave oscillations are investigated in the range of the Strouhal number based on amplitude ( $St_A$ ) from 0.1 to 0.4. The flow velocity is kept constant at  $U = 1.54$  m/s, which corresponds to the chord-based Reynolds number  $Re_c = 2640$ .

### 2.1. Wake Structure

The wake structure was visualized using contours of the  $z$ -component of vorticity ( $\omega_z$ ). The force experienced by the flapping airfoil depends on the wake structure. The wake structure behind the pitching airfoil for different values of  $St_A$  is shown in Fig. 10. The red color denotes positive values of  $\omega_z$  rotating in the anticlockwise direction and the blue color denotes negative values of  $\omega_z$  rotating in the clockwise direction. Two-dimensional numerical investigations on flapping wing identify the wake structure behind the flapping wing by computing the vorticity in the flow field. The snapshots of the vorticity are then used

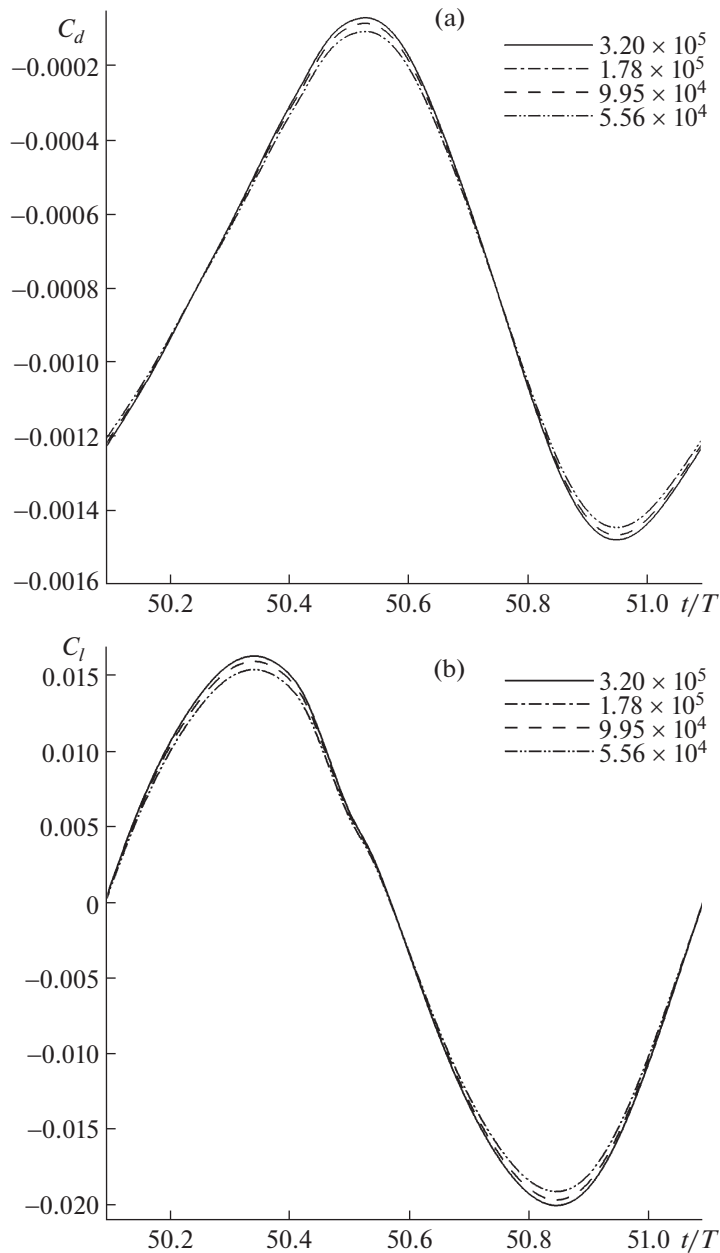


**Fig. 5.** Variation in the coefficients drag (a) and lift (b) over the airfoil with different mesh size.

to present the arrangement of vortices in the wake. The classification of the wake structure is performed basing on the direction of vorticity, which provides the visual idea of vortex street arrangement. This type of visual classification can be difficult in the transition region between the von Kármán and reverse von Kármán streets. The present work identified the vortex street in these transitional areas by computing the vorticity in the vortex cores and comparing it with the wake structure according to [35]. At  $St_A = 0.12$  the vortices produced above and below the airfoil align along the line of symmetry (Fig. 10a); this kind of wake arrangement is called the neutral wake [36]. With increase in  $St_A$  the wake structure arrangement changes, as shown in Fig. 10b. The vortices produced above the airfoil start to arrange below the line of symmetry and vice versa. This arrangement resembles a von Kármán vortex street but with the opposite sense of vorticity, which is called the reverse von Kármán wake. The further increase in  $St_A$  is found to increase the size of the vortices, while the wake arrangement remains unchanged. An increase in the flapping parameter is found to add more strength to the vortices.

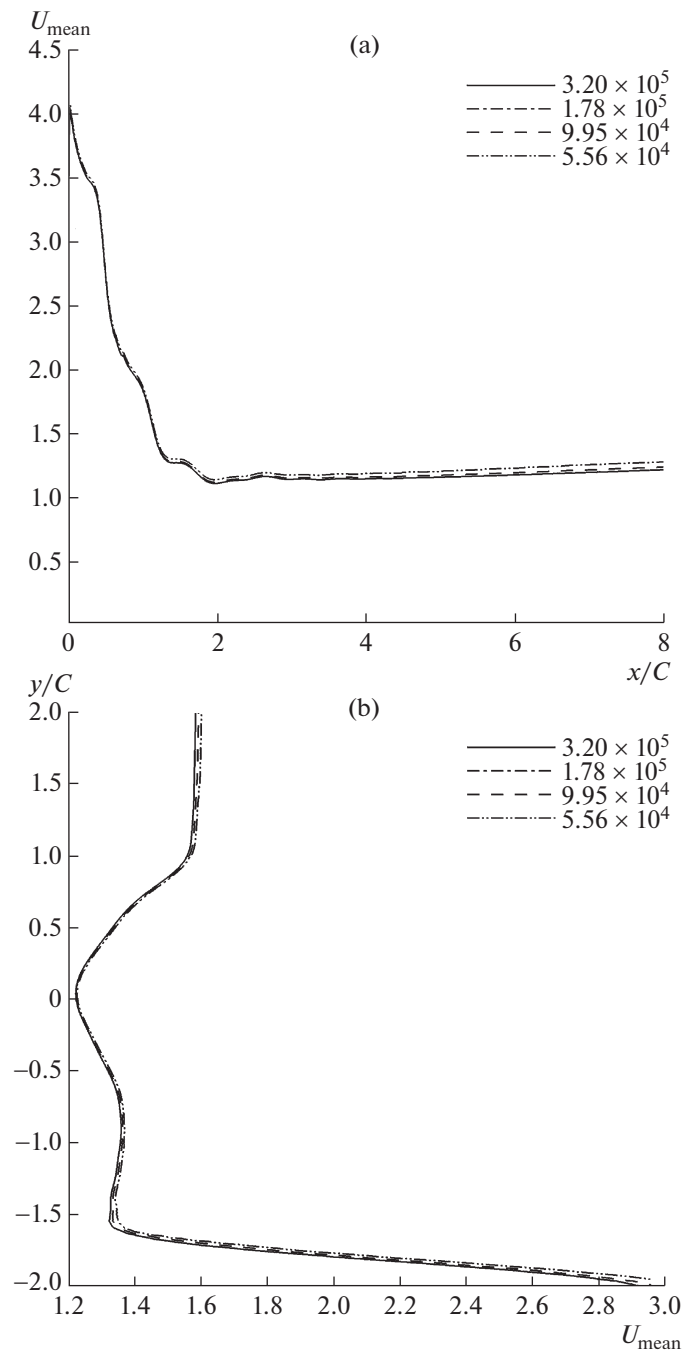


**Fig. 6.** Variation in the mean velocity ( $U_{\text{mean}}$ ) along the line of symmetry (a) and perpendicular to the line of symmetry at  $x = 8C$  (b) with different mesh size.

The wake structure behind the heaving airfoil for different values of  $St_A$  is shown in Fig. 11. A reverse von Kármán street, as shown in Fig. 11a, was observed at  $St_A = 0.12$ . The leading edge vortex separates from the airfoil instead of merging with the trailing edge vortex. The leading edge vortex, significantly smaller in size, diffuses in the flow field, establishing the reverse von Kármán wake. The wake behind the airfoil is found to deflect with increase in  $St_A$  ( $St_A = 0.18$ ), as shown in Fig. 11b. The vortices of opposite sign form a pair just before the wake deflection. The direction of the wake deflection depends on the formation of the vortex pair. The pairing of a clockwise vortex with an anticlockwise vortex generates a dipole that induces an upward motion and results in an upward deflected wake. The pairing of an anticlockwise



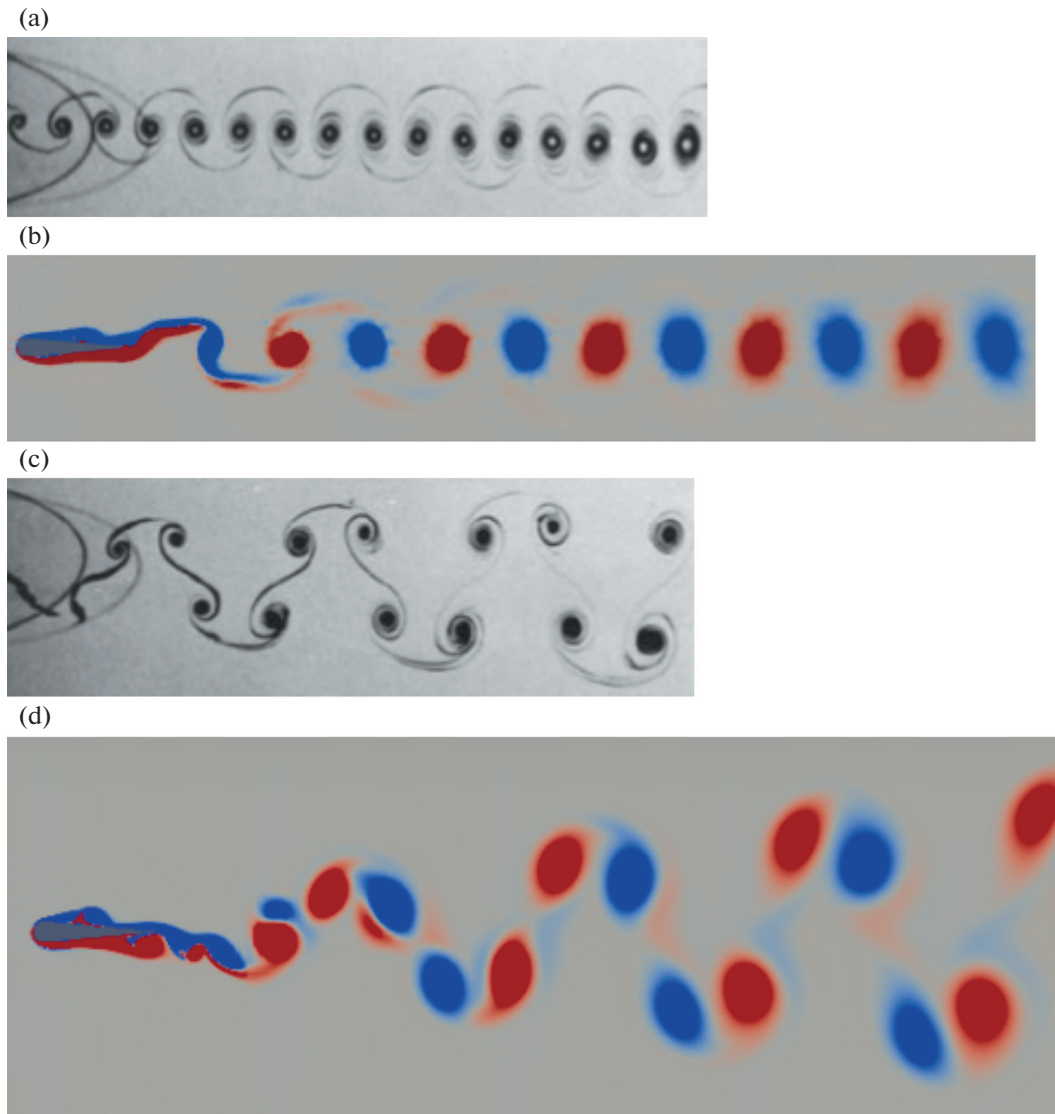


**Fig. 7.** Comparison of the wake patterns obtained numerically (b, d) with the experimental results of Koochesfahani [32] (a, c) for a pitching airfoil at reduced frequencies  $k = 6.7$  (a, b) and  $3.1$  (c, d).

vortex with a clockwise vortex forms another dipole that induces a downward motion resulting in a downward deflected wake. The wake is found to change the direction of deflection with further increase in  $St_A$  to  $0.24$  (Fig. 11c). This phenomenon is called the jet switching [37], where the direction of deflection changes with variation in the flapping parameters. The deflected wake arrangement gets disturbed with further increase in  $St_A$  to  $0.30$  (Fig. 11d). The leading edge vortices produced above the airfoil pass around the leading edge to the bottom side of the airfoil and vice versa. These vortices ultimately get diffused in the flow and do not contribute to the wake structure arrangement. A chaotic wake pattern is observed at  $St_A = 0.36$  (Fig. 11e). The dipoles formed in the chaotic wake are so dispersed that the patterns formed are entirely irregular.

The wake structure behind the pitching-heaving airfoil for different values of  $St_A$  is shown in Fig. 12. The reverse von Kármán type wake arrangement is observed at  $St_A = 0.12$  (Fig. 12a). The vortices are found to increase in size with increase in  $St_A$  (Figs. 12b and 12c). The leading edge vortices separate from the airfoil, proceed slowly toward the trailing edge, and merge with the trailing edge vortices, thus establishing a reverse von Kármán street. The further increase in  $St_A$  to  $0.30$  changes the behavior of the leading edge vortices. The leading edge vortices, instead of merging with the trailing edge vortices, get ejected to

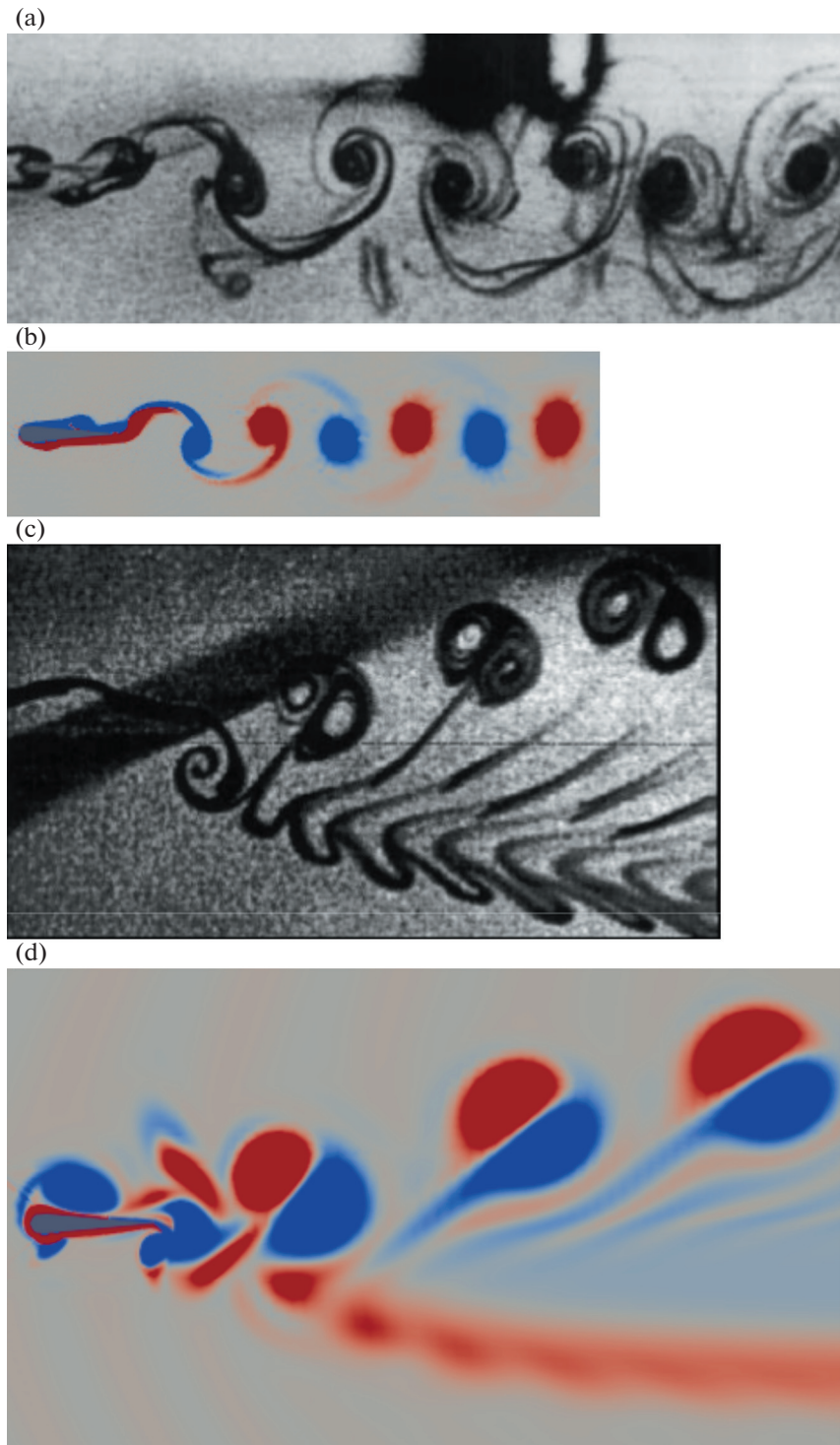


**Fig. 8.** Comparison of the wake patterns obtained experimentally by Jones et al. [14] (a, c) for a heaving airfoil with the same obtained using the present solver (b, d) at reduced frequencies  $k = 3.0$  (a, b) and  $12.5$  (c, d).

the flow and diffuse in the flow with time. An increase in  $St_4$  to  $0.36$  increases the size of the leading edge vortices and the vortices take more time to get diffused in the flow. The leading edge vortices, which are comparatively small in size, stay on the either side of the vortex street produced by the trailing edge vortices. The trailing edge vortices deform the leading edge vortices soon after their ejection into the wake, enhancing the diffusion and establishing the reverse von Kármán street.

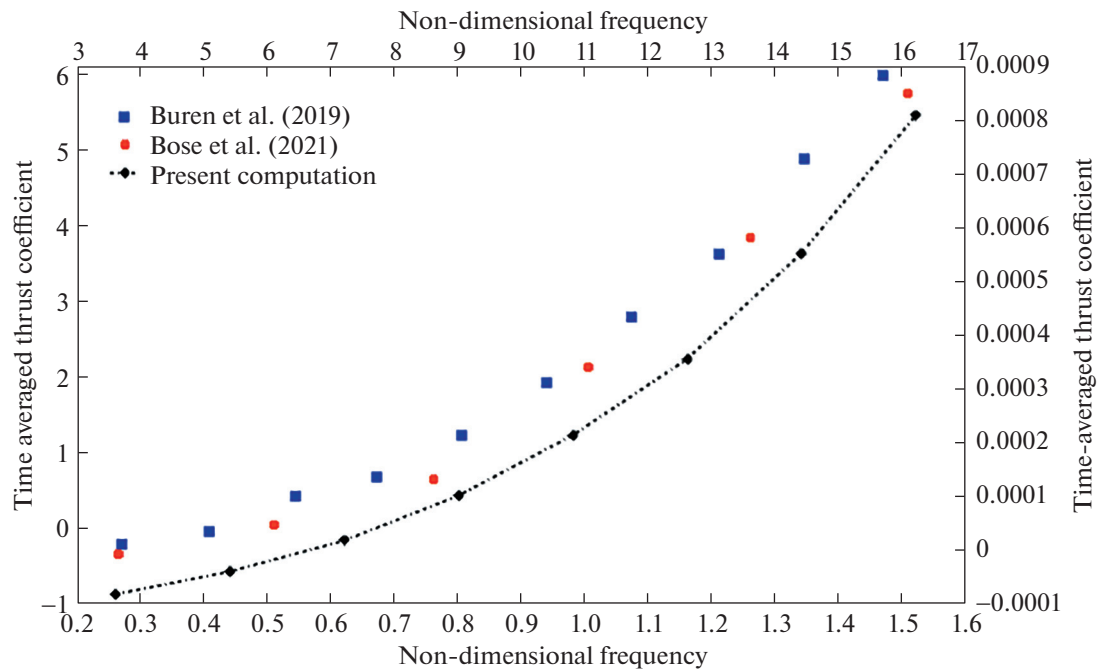


**Fig. 9.** Variation of the thrust coefficient ( $C_t$ ) with the dimensionless flapping frequency ( $f^*$ ) for a simultaneously pitching-heaving airfoil.

### 2.2. Leading and Trailing Edge Vortices

In the present study, the airfoil starts its flapping oscillations from the mean position (shown in Fig. 2), travels to the top-most position, travels back toward the bottom-most position, and finally returns to the mean position, thus completing one cycle. A positive vorticity is developed below the airfoil and a negative vorticity is developed above the airfoil during all three types of flapping oscillations. The vortices are released at the ends of the upstroke and downstroke for all three flapping oscillation configurations. Negative vortices are released at the end of the upstroke and positive vortices are released at the end of the downstroke. Thus, two vortices are produced during one cycle of oscillations and such kind of wake is called a  $2S$  wake. The notation  $S$  corresponds to a single vortex as denoted by Williamson et al. [38].

The leading edge vortex formed during pitching oscillations merges with the trailing edge vortices and establishes a  $2S$  wake in the investigated range of  $St_A$ . But the heaving type oscillations are found to influence the evolution of the leading edge vortex. This will affect the wake structure and hence the force experienced by the airfoil. This influence can be attributed to swift changes in the angle of attack during the heaving oscillations. As a result of this influence, at higher values of  $St_A$  the leading edge vortices, instead of merging with the trailing edge vortices, get released into the flow. However, the leading edge vortices produced are considerably small and diffuse in the flow in the parameter range investigated. Hence the far wake converts to the reverse von Kármán wake. The characteristics of the leading edge vortices generated by combined pitch-heave oscillations remain similar to those of the pitching oscillations at lower  $St_A$  values. But at higher values of  $St_A$  the behavior of the leading edge vortices appears identical to that of the heaving oscillations. It appears that the vortex dynamics of the combined pitch-heave oscillations is governed by the pitching motion at lower values of  $St_A$  and by heaving oscillations at higher values of  $St_A$ .

### 2.3. Deflected Wake

A deflected wake indicates the deviation of the wake vortex arrangement from the line of symmetry. When the wake structure is symmetric about the line of symmetry, the airfoil's resultant force is parallel to the line of symmetry (in the thrust/drag direction). The resultant force developed in a deflected wake will also be inclined to the line of symmetry, which physically implies that the force generated will have components in both lift and thrust directions. Thus, the parameter range over which the deflected wakes exist is practically relevant. In the present study, the flapping parameter is gradually increased to identify the parameter value at which the wake behind the airfoil deflects for each type of flapping oscillations.

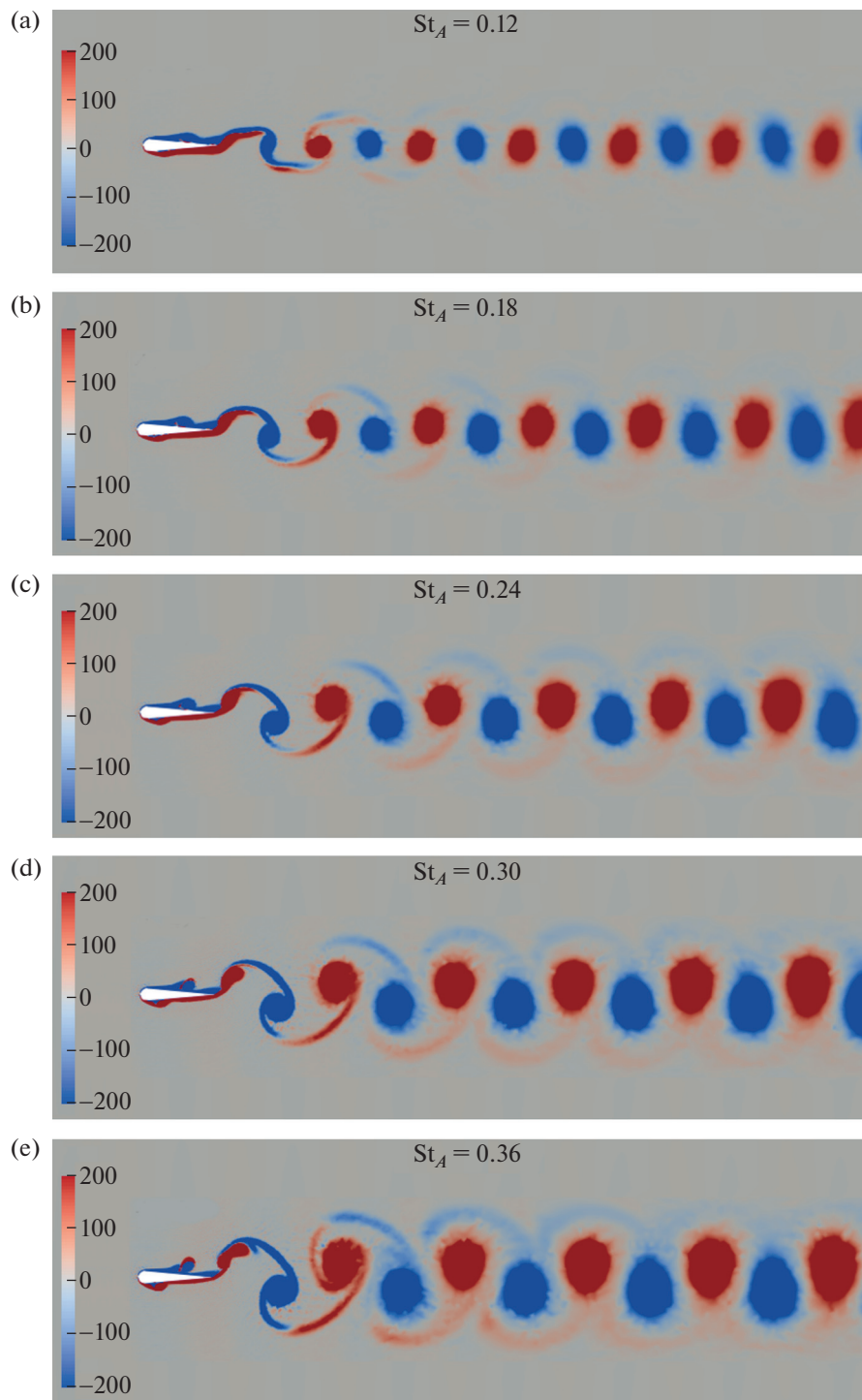


**Fig. 10.** Wake structure behind the pitching airfoil visualized using the  $z$ -component of vorticity ( $\omega_z$ ). The red color represents anticlockwise rotating positive vortices and the blue color represents the clockwise rotating negative vortices.

Figure 13 shows the deflected wake obtained behind each type of flapping oscillations. The wake behind the pitching airfoil is found to deflect around  $St_A = 0.39$ , while the wake behind the heaving airfoil deflects much earlier, around  $St_A = 0.18$ . The wake behind the airfoil undergoing combined pitch-heave oscillations deflects at a comparatively higher value of  $St_A$ , around 0.27. The deflection in the wake behind the airfoil in combined pitch-heave motion occurs at  $St_A$  value lower than the  $St_A$  at which deflection

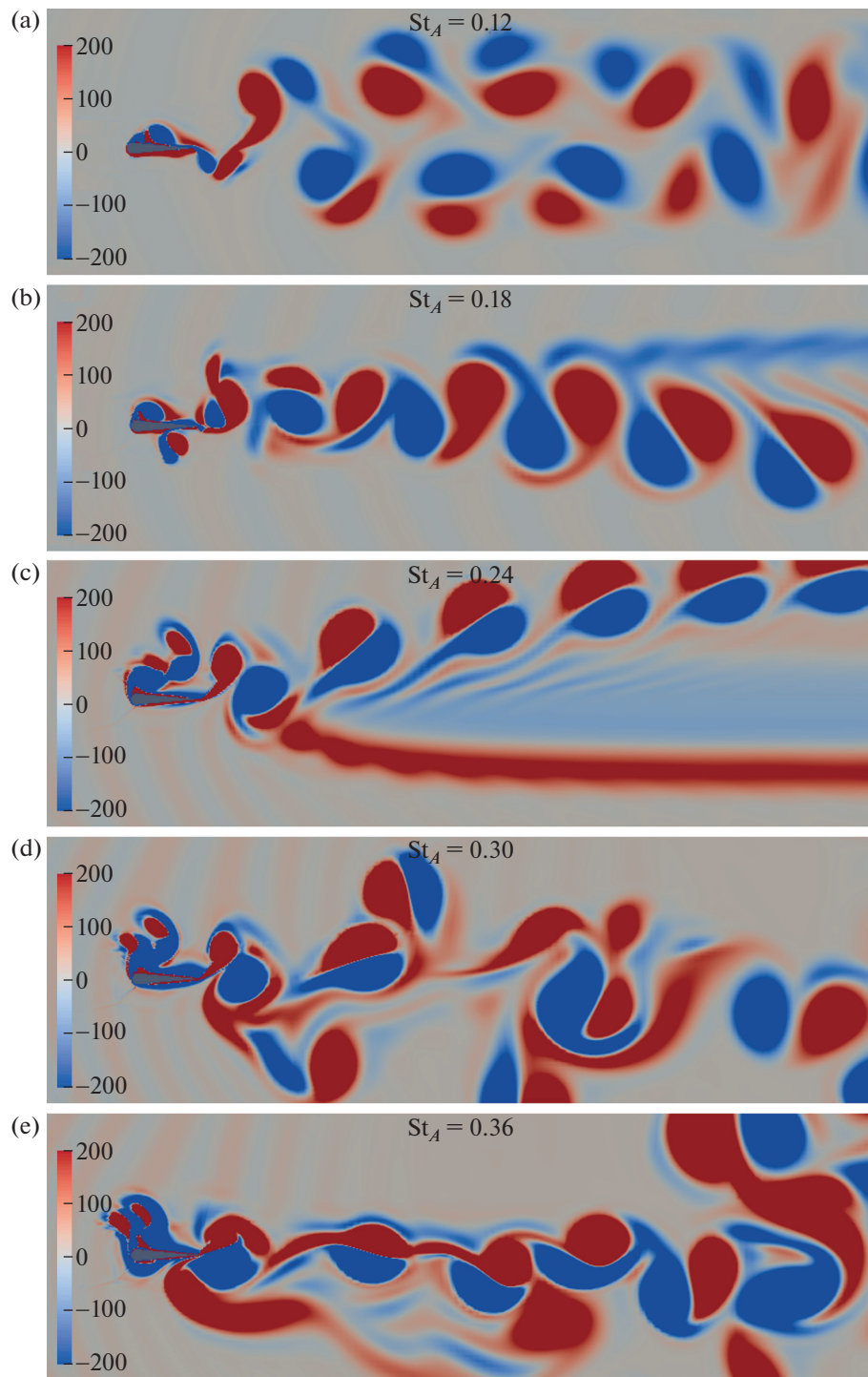


**Fig. 11.** Wake structure behind the heaving airfoil visualized using the  $z$ -component of vorticity ( $\omega_z$ ). The red color represents anticlockwise rotating positive vortices and the blue color represents the clockwise rotating negative vortices.

occurs for a pitching airfoil. This occurs due to the influence of heaving oscillations on the airfoil performing combined pitch and heave. It also confirms the observation that the vortex dynamics of the combined pitch-heave oscillations is governed by the pitching oscillations at lower values of  $St_A$  and by the heaving oscillations at higher values of  $St_A$ .

At this point, it is worth mentioning the instabilities that initiate the formation of the deflected wake (symmetry breaking). A stability analysis (Dyannikova et al. [39]) showed that the symmetry breaking of a

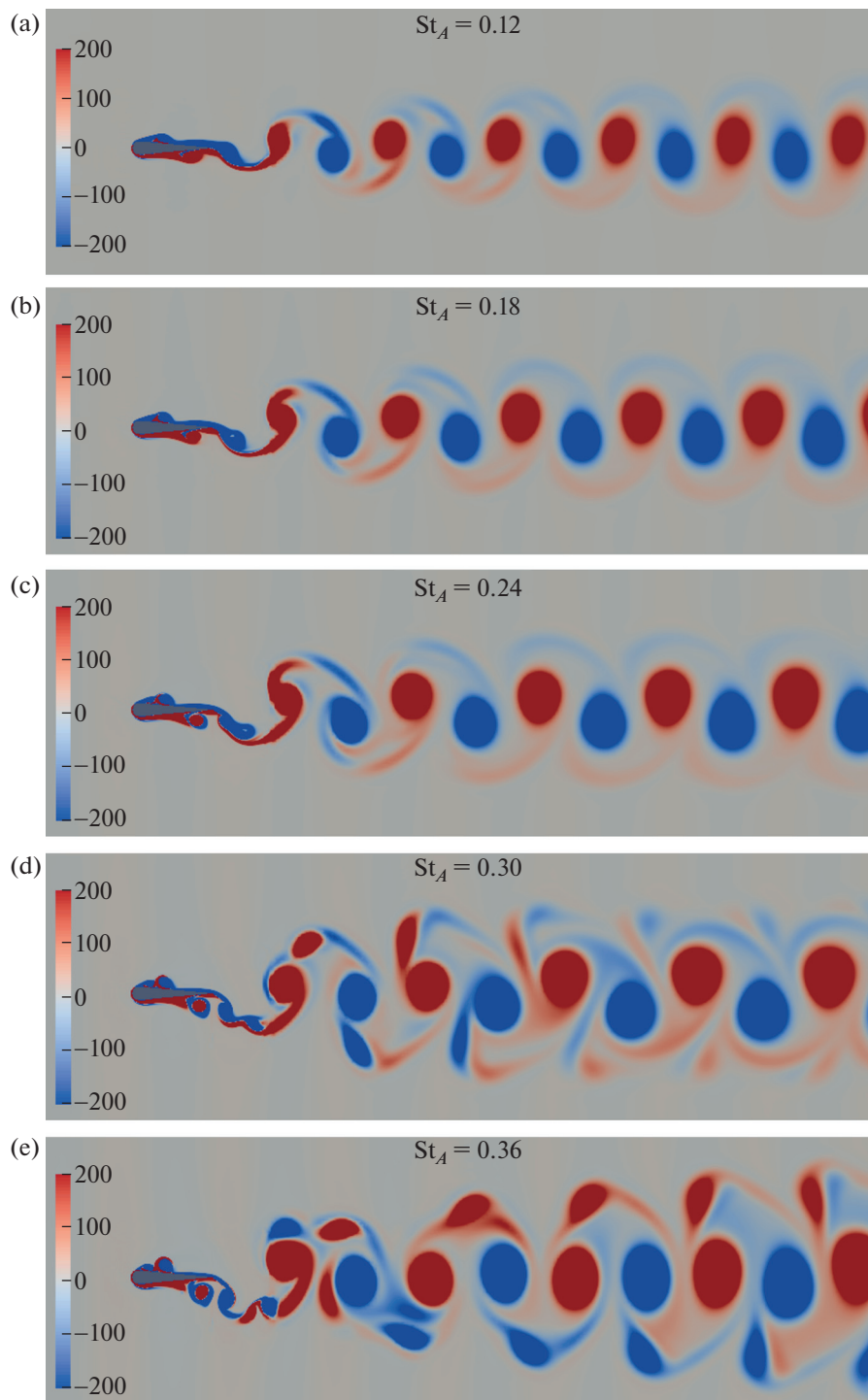


**Fig. 12.** Wake structure behind the pitching-heaving airfoil visualized using the  $z$ -component of vorticity ( $\omega_z$ ). The red color represents anticlockwise rotating positive vortices and the blue color represents the clockwise rotating negative vortices.

von Kármán street is caused by varicose perturbations, whereas the symmetry breaking of a reverse von Kármán street is caused by bending perturbations [40]. The pairing of vortices results in the formation of a dipole and the resulting moment from the dipole can act as a bending instability on the symmetric reverse von Kármán street. Thus, the dipole formation can be considered as a factor affecting the onset of a deflected wake. It was already mentioned in the previous section (Subsection 2.1) that the deflection direction is determined by the order in which the vortex pairing occurs.

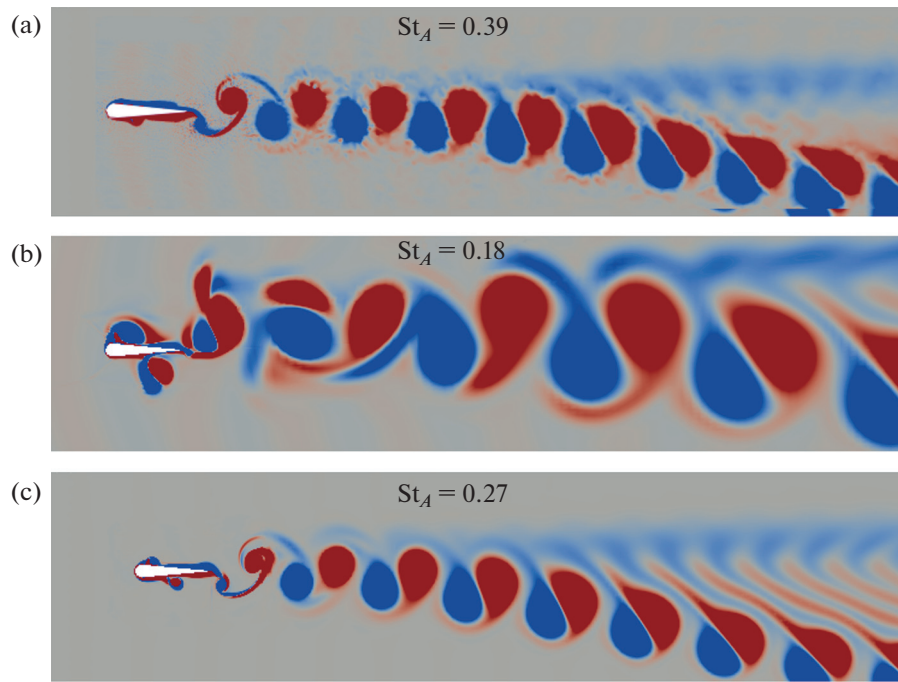


**Fig. 13.** Deflected wake obtained for different types of flapping oscillations (pitching (a), heaving (b), and combined pitch-heave (c)). The red color represents anticlockwise rotating positive vortices and the blue color represents the clockwise rotating negative vortices.

#### 2.4. Aerodynamic Forces

The force experienced by the airfoil depends on the wake structure. A drag wake corresponds to the wake, where the airfoil experiences a drag force, and a thrust wake corresponds to the wake, where the airfoil experiences a thrust force. The wake structure corresponding to a drag wake resembles a von Kármán vortex street, whereas the wake structure corresponding to a thrust wake resembles a reverse von Kármán vortex street. In the present study, the average force experienced by the airfoil undergoing different types of oscillations is computed and a comparison is presented. The force data for averaging are gathered after removing the initial transient data. Figure 14a shows the variation of the thrust coefficient ( $C_t$ ) with an increase in the Strouhal number based on the amplitude ( $St_A$ ) for different types of flapping oscillations. The negative values of  $C_t$  correspond to the drag coefficient. The heaving airfoil is found to experience the thrust force for all values of  $St_A$  under investigation. However, transition to a chaotic wake (Figs. 11d and 11e) restricts an increase in the thrust force with increase in  $St_A$ . The pitching and combined-motion airfoils experience the drag force at  $St_A = 0.12$ . But the corresponding wake structure arrangement is a reverse von Kármán street (Figs. 10a and 12a) which shows that the existence of a reverse von Kármán street is not sufficient to identify a thrust wake. The drag force is found to transform to the thrust force with increase in  $St_A$ . The behavior of the aerodynamic force experienced by the airfoil in combined pitch and heave follows the trend exhibited by the pitching airfoil at lower values of  $St_A$  and the trend exhibited by the heaving airfoil at higher values of  $St_A$ . The drag-to-thrust transition for the pitching airfoil is observed around  $St_A = 0.18$ . However, the transition in the wake structure arrangement occurs much earlier, i.e., the wake transition is found to precede the transition from drag to thrust.

The maximum streamwise velocity ( $U_{\max}$ ) in the wake behind the flapping airfoil is an important parameter, as it influences the maximum force experienced by the airfoil. The influence of the flapping parameters on  $U_{\max}$  is quantified for different flapping oscillations and is presented in the dimensionless form. The  $U_{\max}$  is normalized by the oncoming flow velocity ( $U$ ) to obtain the dimensionless form. Figure 14b shows the variation of  $U_{\max}/U$  with increase in  $St_A$ . The dependence is plotted at location  $x = 2C$  from the trailing edge. This location is chosen basing on the observation that the influence of the flapping airfoil will diminish in the far wake [35]. The  $U_{\max}/U$  values are highest for the heaving oscillations and lowest for the pitching oscillations. The value of  $U_{\max}/U$  is almost the same for different types

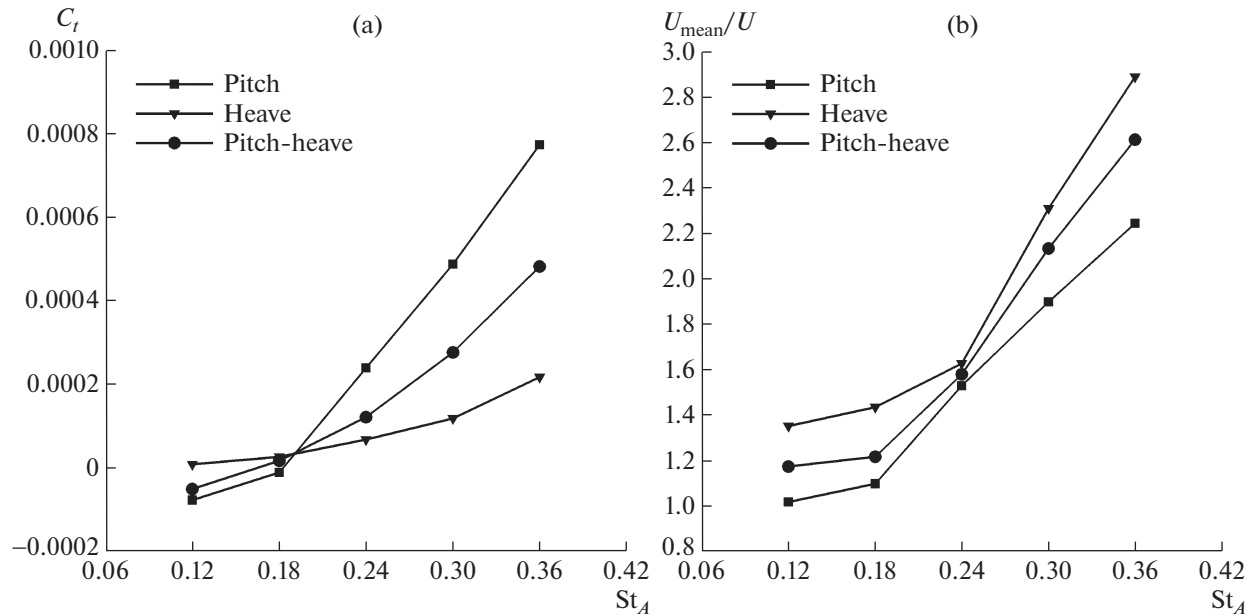


Fig. 14. Variation of the thrust coefficient ( $C_t$ ) (a) and  $U_{\max}/U_0$  (b) with the Strouhal number based on the amplitude ( $St_A$ ).

of oscillations at  $St_A = 0.24$ . The behavior of  $U_{\max}/U$  in the combined pitch-heave oscillations adheres closely to the behavior of  $U_{\max}/U$  in the pitching oscillations, when  $St_A$  is below 0.24, and resembles more like the behaviour of  $U_{\max}/U$  in the heaving oscillations, when  $St_A$  is above 0.24. Thus,  $St_A = 0.24$  can be considered as the critical value around which the influence of pitch oscillations or heave oscillations alters for the airfoil undergoing combined pitch-heave oscillations.

**2.4.1. Interdependence of the wake arrangement and the forces generated.** Table 1 gives the wake classification based on the force experienced by the airfoil for different types of flapping oscillations. A drag wake produces a drag force on the airfoil, while a thrust wake provides a thrust force to the airfoil. A neutral wake implies the condition, where the airfoil experiences neither thrust nor drag. The vorticity contour plot for a pitching airfoil shows that the wake arrangement corresponding to  $St_A = 0.12$  is similar to that of a neutral wake (Fig. 10a) and the wake arrangement corresponding to  $St_A = 0.18$  is similar to that of a reverse von Kármán wake. A neutral wake is expected to produce zero force on the airfoil. On the other hand, a reverse von Kármán wake is expected to provide a thrust force. However, the computed force indicates that the airfoil experiences a drag force at both  $St_A$  values. This conundrum between the wake structure and the force experienced is also found for an airfoil in combined motion at  $St_A = 0.12$ . This implies that at low values of the flapping parameters the structural arrangement of the wake does not need to be indicative of the force experienced by the airfoil. Essentially that there will be a critical value of  $St_A$  above which the wake arrangement and the force experienced by the airfoil will be interdependent and below that critical value the force experienced by the airfoil is not predictive based on the wake arrangement. The data of Table 1 indicate that the critical value is different for different types of flapping oscillations.

## 2.5. Reynolds Stresses

The transient variables in a periodic flow comprise mean, periodic, and random components [41]. Mathematically, this can be expressed as follows:

$$\phi = \bar{\phi} + \phi' + \tilde{\phi}, \quad (2.1)$$

where  $\phi$  is the transient variable,  $\bar{\phi}$  is the mean component,  $\phi'$  is the periodic component, and  $\tilde{\phi}$  is the random component. The mean component ( $\bar{\phi}$ ) and the periodic component ( $\phi'$ ) are inherent in both laminar and turbulent flows but the random component ( $\tilde{\phi}$ ) exists only in turbulent flows. The random component ( $\tilde{\phi}$ )



**Table 1.** Wake classification based on the force experienced by the airfoil undergoing different flapping oscillations for different values of  $St_A$ 

$St_A$	Pitching	Heaving	Combined pitch-heave
0.12	Drag wake	Thrust wake	Drag wake
0.18	Drag wake	Thrust wake	Thrust wake
0.24	Thrust wake	Thrust wake	Thrust wake
0.30	Thrust wake	Thrust wake	Thrust wake
0.36	Thrust wake	Thrust wake	Thrust wake

does not exist in the present laminar analysis and, hence, the periodic component ( $\phi'$ ) is used to formulate the stress components. The normal averaged stress in the  $x$  and  $y$  directions are presented as  $\overline{u'u'}$  and  $\overline{v'v'}$ , respectively.

Figure 15 presents the contours of  $\overline{u'u'}$  for different types of flapping motion with variation in  $St_A$ . At  $St_A = 0.12$  the  $\overline{u'u'}$  contours exhibit a symmetric pattern for the three types of flapping oscillations (Figs. 15a–15c) indicating the periodicity in the flow. The contours of  $\overline{u'u'}$  bifurcate into two halves about the line of symmetry after the trailing edge. The heaving motion develops a maximum value of  $\overline{u'u'}$  ( $(\overline{u'u'})_{\max}$ ) near the leading edge (Fig. 15b), where the flow experiences a maximum disturbance, and the leading edge vortex significantly influences the Reynolds stress component. In contrast, the pitching motion develops a maximum value close to the trailing edge (Fig. 15a), since the flow undergoes less disturbances near the leading edge and the influence of the leading edge vortex is comparatively small. The heaving motion generates a significant amount of stress in the flow field (Fig. 15b) compared to the other types of flapping oscillations (Figs. 15a and 15c). The  $\overline{u'u'}$  distribution for the combined oscillation is governed by the interaction between the pitching and heaving oscillations.

The quantity  $\overline{u'u'}$  increases with increase in  $St_A$  (Figs. 15d–15f). A small change in  $St_A$  brings a significant change in the  $\overline{u'u'}$  field. The increase in magnitude of  $\overline{u'u'}$  with  $St_A$  appears to be of the same order for all types of flapping oscillations. The peak values of  $\overline{u'u'}$  are found in the path through which the vortex propagates. The peak values of  $\overline{u'u'}$  found on both sides of the line of symmetry indicate rotation of the fluid about the mean flow [41]. The quantity  $\overline{u'u'}$  is almost zero along the line of symmetry, since no vortex propagates through that path. The  $\overline{u'u'}$  contours for the heaving airfoil are found to deflect in the far wake (Fig. 15e), similarly to the vorticity contours (Fig. 11b). However, no deflection is observed in the wake behind the pitching airfoil (Fig. 15d) and the airfoil in combined motion (Fig. 15f). The further increase in  $St_A$  to 0.36 brings a dynamic increase in the magnitude of  $\overline{u'u'}$  for the heaving motion (Fig. 15h) compared to the other types of flapping motion (Figs. 15g and 15i). The deflected wake behind the heaving airfoil at  $St_A = 0.36$  (Fig. 15h) indicates the aperiodicity developed in the flow.

Figure 16 shows the contours of  $\overline{v'v'}$  for different types of flapping motion with variation in  $St_A$ . The magnitude of  $\overline{v'v'}$  is higher than the magnitude of  $\overline{u'u'}$  for each  $St_A$ . Similarly to  $\overline{u'u'}$ , a maximum value of  $\overline{v'v'}$  ( $(\overline{v'v'})_{\max}$ ) for the heaving airfoil is observed close to the leading edge (Fig. 16b). Whereas, the location of  $(\overline{v'v'})_{\max}$  for the other two types of flapping oscillations is obtained close to the trailing edge (Figs. 16a and 16c). The peak values of  $\overline{v'v'}$  are obtained along the line of symmetry instead of locations on its either side as observed for  $\overline{u'u'}$ . This implies that the peak values of  $v'$  (both positive and negative) at any section exist at the line of symmetry. With increase in  $St_A = 0.18$ , the location of  $(\overline{v'v'})_{\max}$  is found to move away from the trailing edge (Figs. 16d and 16f) for the airfoil in the pitching and combined motions. This is the location, where the vortices cross the line of symmetry to establish the reverse von Kármán street. The location of  $(\overline{v'v'})_{\max}$  remains close to the leading edge for the heaving airfoil (Fig. 16e) indicating the significance of the leading edge vortex in the heaving conditions. The distance between the airfoil's

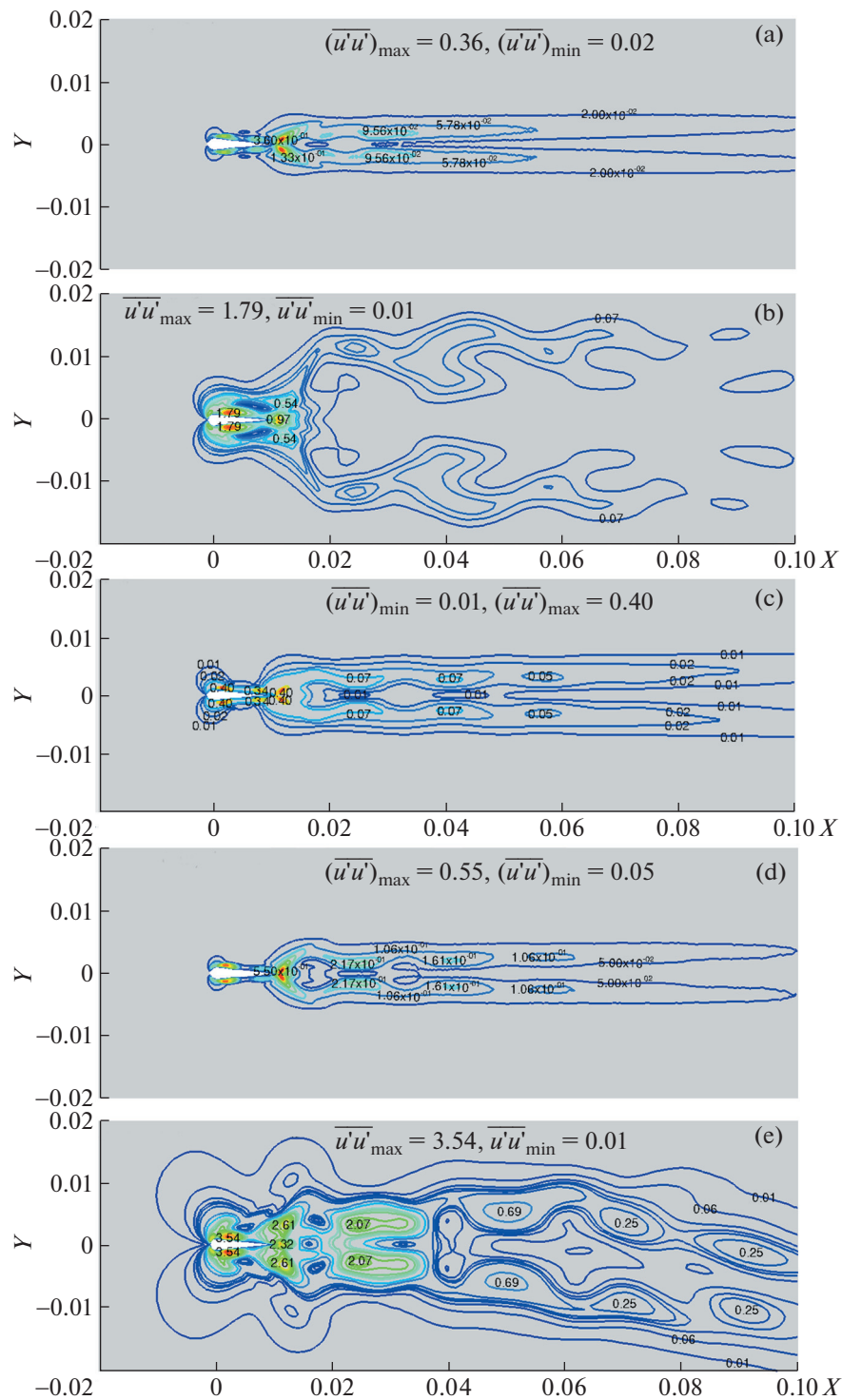


**Fig. 15.** Contours of  $\overline{u'u'}$  behind the airfoil for different types of flapping oscillations (pitching (a, d, g), heaving (b, e, h), and combined (c, f, i)) at  $St_A = 0.12$  (a–c), 0.18 (d–f), and 0.36 (g–i).

trailing edge and the location of  $(\overline{v'v'})_{max}$  increases with increase in  $St_A$  (Figs. 16g and 16h). The trailing edge vortices become more prominent with increase in  $St_A$  and their separation from the airfoil is delayed. The delay in vortex separation from the trailing edge makes the vortices to release at locations far away (in the  $y$  direction) from the line of symmetry. Therefore, the vortices cross the line of symmetry at locations further away from the trailing edge and hence the displacement of the  $(\overline{v'v'})_{max}$  location. Figure 16b confirms the aperiodicity developing in the flow with increase in  $St_A$ .

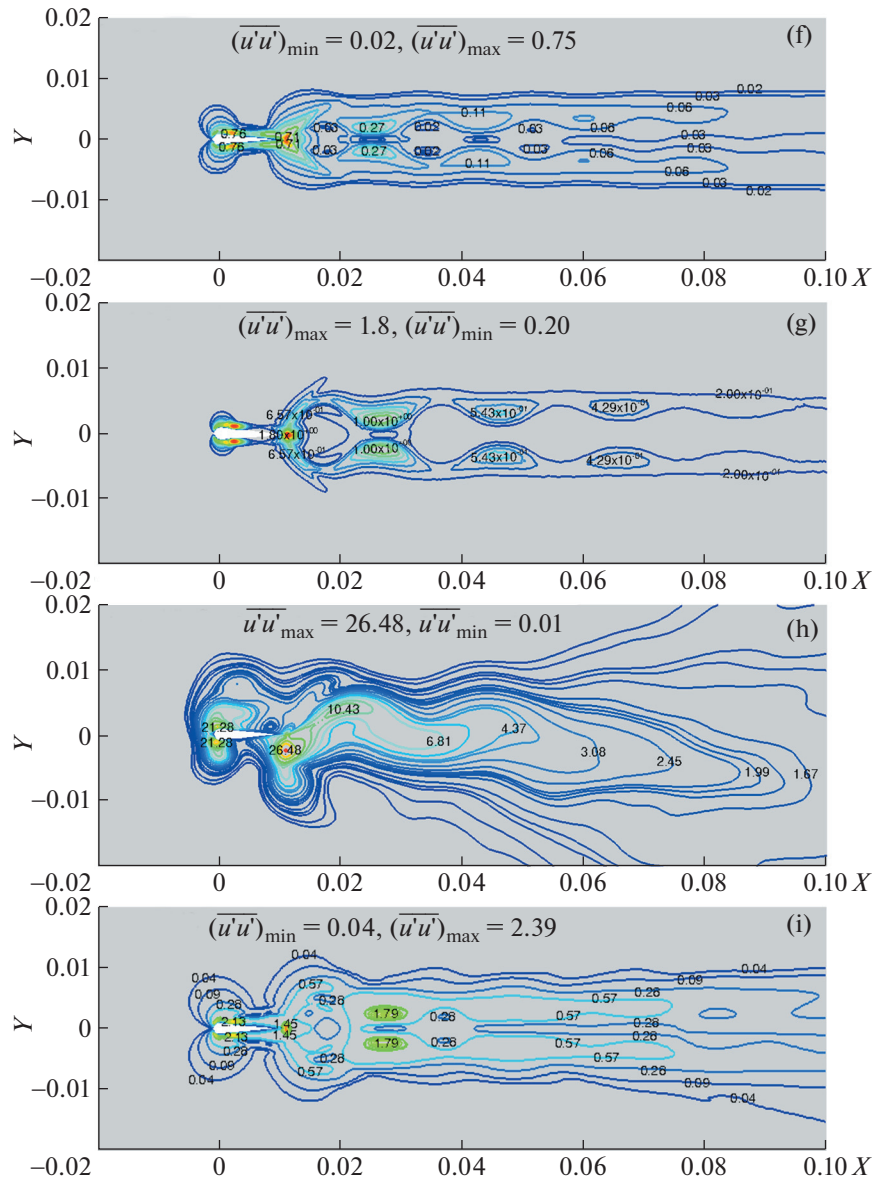
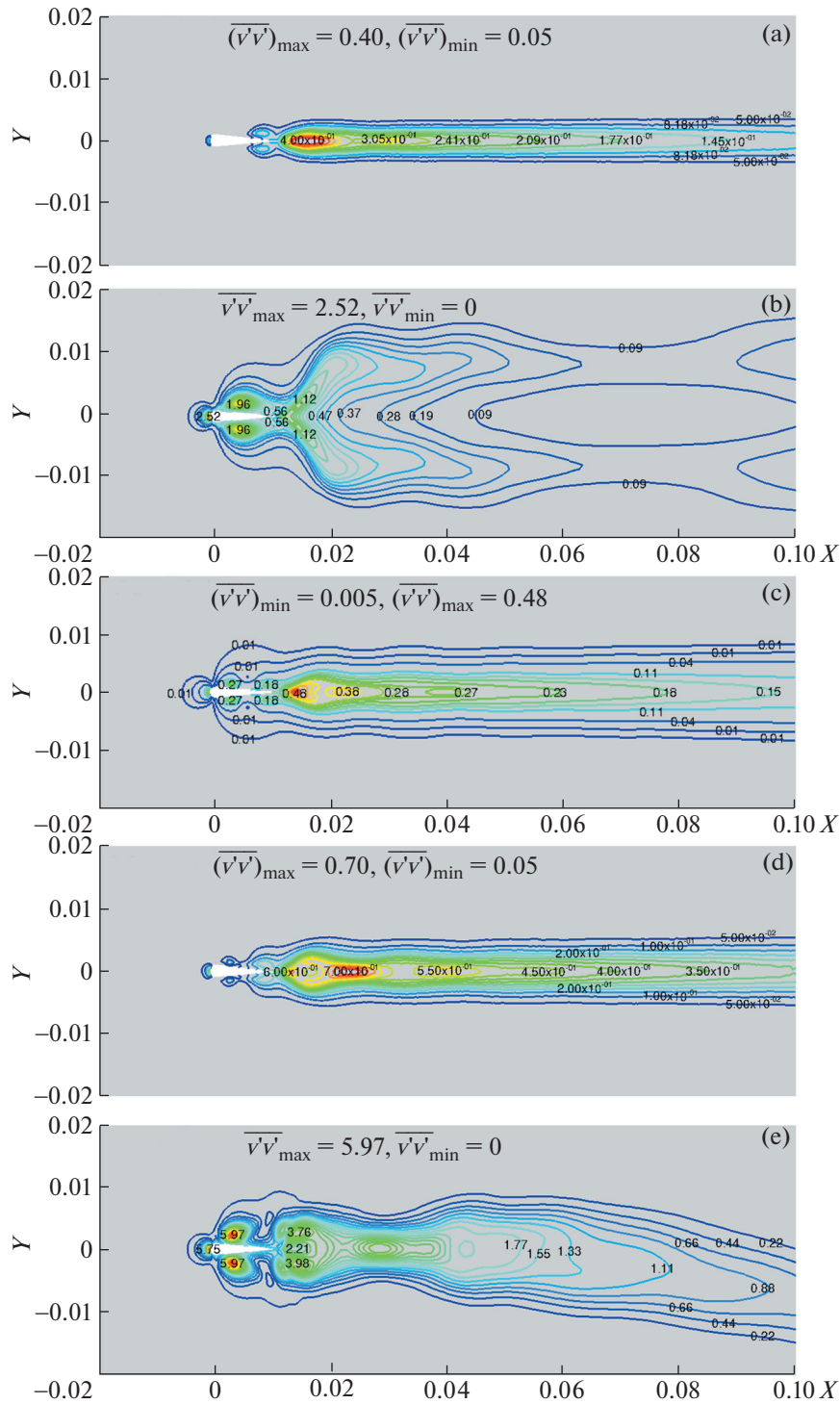


Fig. 15. (Contd.).

The high values of  $\overline{u'u'}$  and  $\overline{v'v'}$  in the near wake indicate a significant amount of fluid mixing. However the magnitudes of  $\overline{u'u'}$  and  $\overline{v'v'}$  decrease, as the flow proceeds, because of kinetic energy dissipation. The stress contour plots show that the greatest stress is observed for the heaving airfoil followed by the airfoil in combined motion. The stress developed is minimum in the case of the pitching airfoil. The obstruction generated to the flow by the flapping airfoil during flapping motion governs the stress distribution in the flow field. The energy dissipated into the flow from the flapping airfoil is maximum for heaving motion and minimum for pitching motion. The stress contour plots also show that the periodic velocity fluctuations are correlated throughout the flapping cycle and contribute significantly to the flow via the stress components developed in the flow field.

### 2.6. Proper Orthogonal Decomposition

The underlying coherent structures in the wake of the flapping airfoil are examined using the proper orthogonal decomposition (POD). The proper orthogonal decomposition breaks down the flow field into multiple orthogonal modes based on the energy captured. These modes are analyzed to understand the



**Fig. 16.** Contours of  $\overline{v'v'}$  behind the airfoil for different types of flapping oscillations (pitching (a, d, g), heaving (b, e, h), and combined (c, f, i)) at  $St_A = 0.12$  (a–c), 0.18 (d–f), and 0.36 (g–i).

subsisting features of the flow. The method of snapshots developed by Sirovich [42] is employed to perform the proper orthogonal decomposition analysis. In the snapshot method, the velocity field is expressed in terms of eigen modes as follows:

$$u(x, t) = \sum_{n=1}^N a_n(t) \phi_n(x),$$

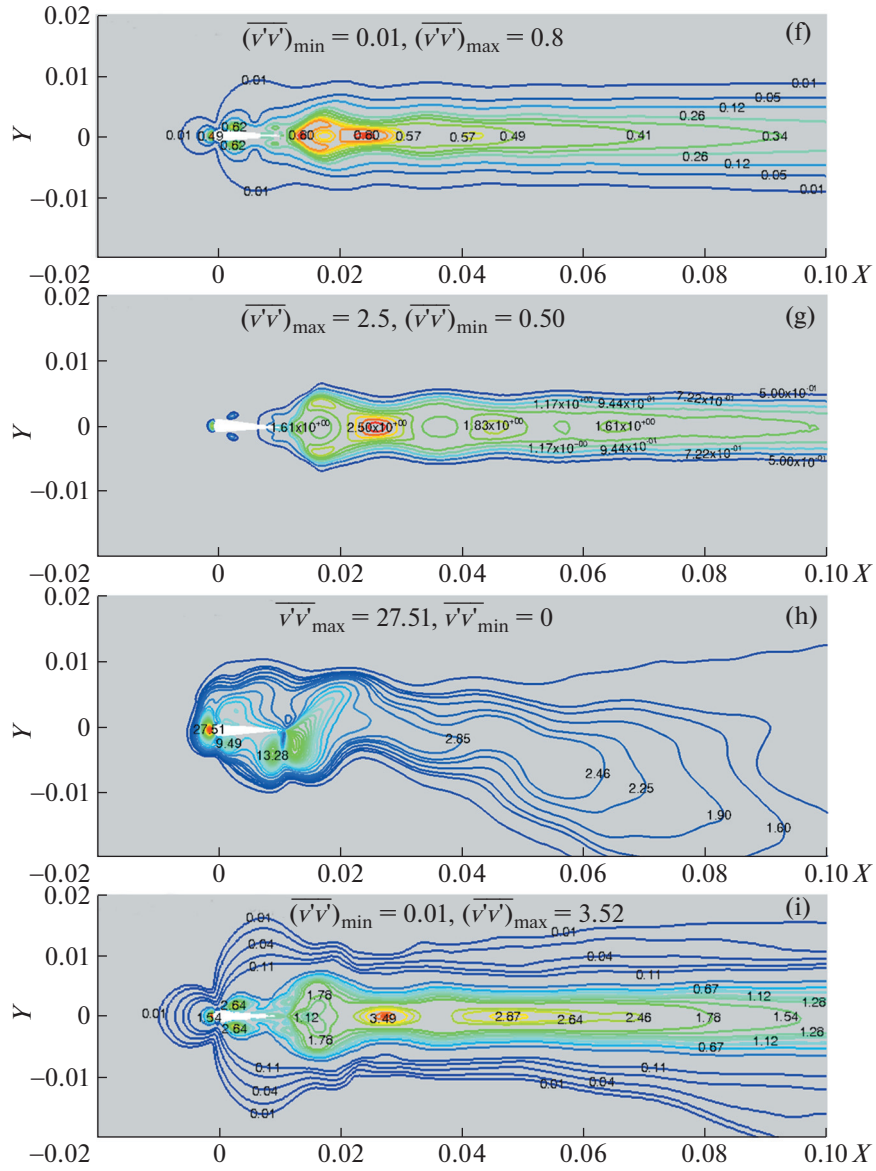


Fig. 16. (Contd.).

where  $\phi_n(x)$  denotes the orthogonal eigenmodes,  $a_n(t)$  are the temporal coefficients, and  $n$  is the snapshot number. The variable  $N$  denotes the total number of snapshots used to extract the POD modes. The statistical stationarity is ensured by using a sufficiently high number of snapshots.

The velocity matrix  $R$  is constructed with the velocity snapshots  $(u_1, u_2, \dots, u_N)$  collected from time instants  $t_1, t_2, \dots, t_N$

$$R = [u_1, u_2, \dots, u_N].$$

The matrix  $U$  will have velocity snapshots as its columns. Then the eigenvectors  $(u_j)$  and the eigenvalues  $(\lambda_j)$  are computed for the correlation matrix

$$S = R^T R.$$

Using the eigenvectors  $(u_j)$  of the velocity matrix and the eigenvalues  $(\lambda_j)$  the POD modes are calculated according to the formula

$$\phi_j = Uu_j/\sqrt{\lambda_j}.$$

The eigenvalues correspond to the kinetic energy captured by each mode. Usually, the correlation matrix  $S$  is of the size  $m \times m$  (where  $m$  is the number of the gridpoints) which requires high computational powers for calculating the eigenvectors. The snapshot method's advantage is that the number of snapshots ( $n$ ) required is much smaller than the number of the gridpoints ( $n \ll m$ ). So the solution of the  $n \times n$  matrix in calculating the eigenvectors offers a significant computational advantage.

**2.6.1. Coherent structures.** The POD analysis is performed in a small domain of size  $9C \times 4C$ , as shown in Fig. 2. The size of the domain is chosen such that the near wake dynamics can be effectively captured. The method of snapshots is performed by collecting 640 snapshots at equal intervals over 20 consecutive flapping cycles. A comparative study of the POD analysis for the flapping oscillations considered is performed for different values of  $St_A$ . The most energy-containing mode of POD (mode 1) is used to perform the comparative study. Figure 17 presents the POD mode 1 behind the flapping wing performing pitching (on the left) and heaving (on the right) oscillations. The coherent structures are arranged in an anti-symmetric pattern about the line of symmetry, i.e., the structures of opposite sense of rotation appear alternately on both sides of the line of symmetry.

The coherent structures behind the pitching airfoil appear to be more compact and rugged (Fig. 17a) but the coherent structures appear to be more distributed for the heaving airfoil (Fig. 17b). The distributed arrangement can be attributed to the higher energy transfer from the heaving airfoil to the fluid in flow. The coherent structures behind the pitching airfoil appear to move apart from each other with increase in  $St_A$  (Figs. 17c, 17e, 17g, 17i). However the structures do not exhibit any indication of transition toward aperiodicity. The coherent structures behind the heaving airfoil deflect (Fig. 17d) as soon as the wake deflection occurs. But the comparatively lower energy-carrying modes do not display any deflection (not presented here) suggesting that the lower energy-carrying structures remain unaffected by increase in  $St_A$ . This indicates that a deflected mean flow itself contains structures, whose characteristics are entirely different from the mean flow [43]. The further increase in  $St_A$  to 0.24 produces a deflection in the higher energy carrying mode (Fig. 17f), as well as the lower energy carrying modes and all the POD modes are representative of the mean flow nature. At  $St_A = 0.30$  the aperiodicity developed in the flow is found to influence the evolution of the coherent structures (Figs. 17h and 17j). The structures in the flow field get distributed randomly and become completely unpredictable. The coherent structures behind the flapping wing are not presented here for brevity. The structures observed are qualitatively similar indicating the periodicity of the flow.

## SUMMARY

The uniform incompressible two-dimensional laminar flow past an airfoil executing different types of flapping oscillations is investigated. The investigation is performed at a constant Reynolds number,  $Re_c = 2640$ , and the results are presented for the Strouhal numbers  $St_A$  varying from 0.1 to 0.4. A comparison of the wake characteristics for pitching, heaving, and combined oscillations is presented. The flapping motion develops positive and negative vorticity below and above the airfoil surface, respectively. The mechanism of vortex generation is found to be similar for all the three types of flapping oscillations and seems to depend on the initial direction of the airfoil motion. The reverse von Kármán type wake, the deflected wake, and the chaotic wake are observed for different flapping parameters considered in this study. The wake behind the heaving airfoil deflects from its symmetric nature much earlier compared to the other two types of flapping oscillations. This wake deflection is linked to the evolution of the leading edge vortices. The dipole formation can be considered as a factor affecting the onset of wake deflection. It is generally perceived that the formation of a reverse von Kármán wake corresponds to a thrust wake, where the airfoil experiences a thrust force. However, the force measurements show that the formation of reverse von Kármán wake arrangement precedes the thrust generation on the airfoil.

The vortex dynamics of the combined oscillations appear to be governed by the pitching motion at lower values of  $St_A$  and by heaving oscillations at higher values of  $St_A$ . The velocity measurements in the wake suggest that the transition of the influence between pitch and heave appears around  $St_A = 0.24$ . The force measurements indicate that there must be a critical value of  $St_A$  below which the wake arrangement and the force experienced by the airfoil will be interdependent. The periodic component of velocity fluctuations is found to develop a non-isotropic stress field around the flapping airfoil in the parameter range considered. The  $\overline{v'v'}$  appears to be dominant in the wake of the flapping airfoil, as compared to the  $\overline{u'u'}$ . The stress components suggest that an increase in  $St_A$  has a greater effect on the heaving airfoil compared to the other two types of flapping oscillations. The stress components also show that the energy transferred from the flapping airfoil to the fluid is maximum for the heaving airfoil followed by the airfoil in combined

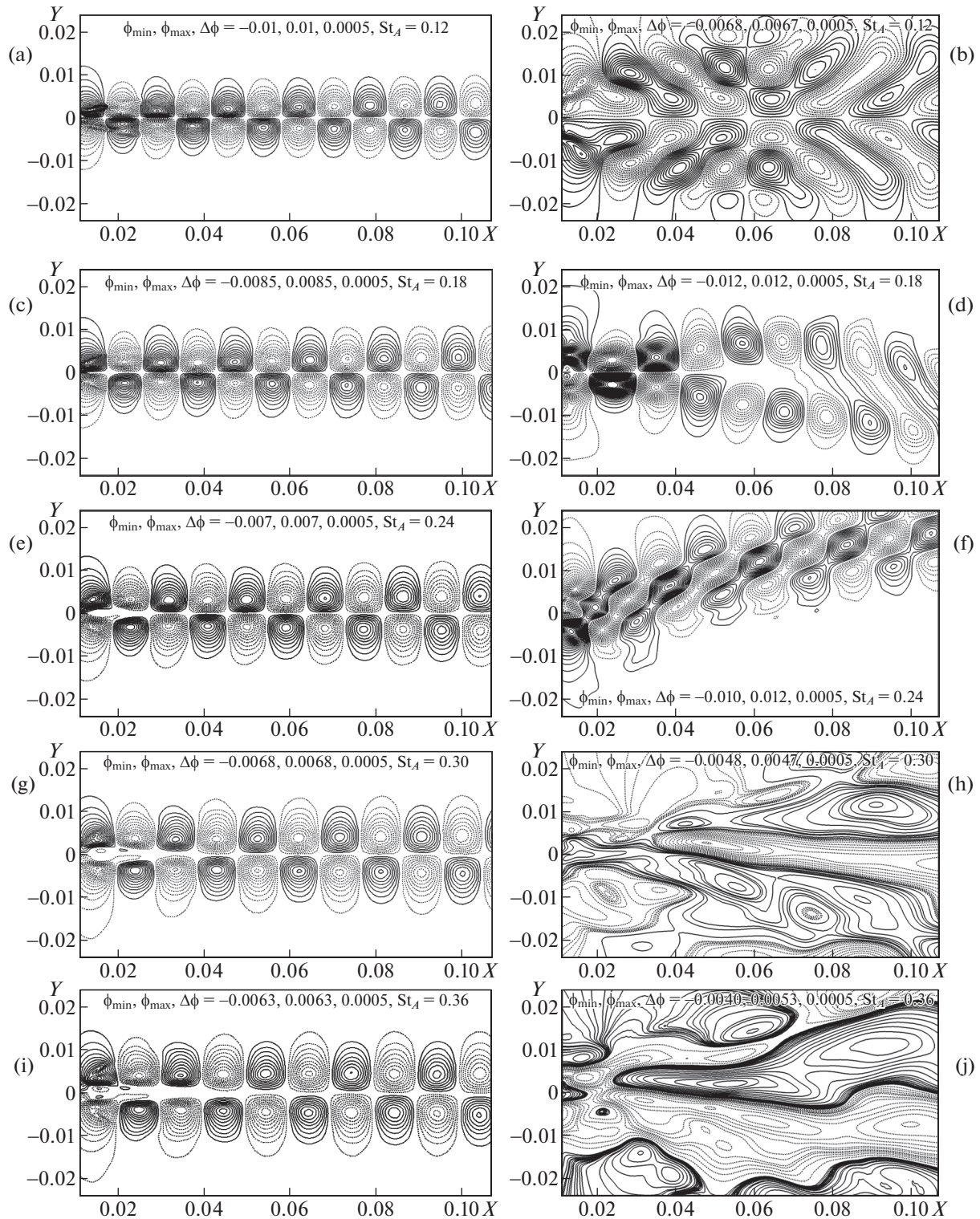


Fig. 17. Coherent structures in the wake behind the pitching airfoil (on the left) and the heaving airfoil (on the right) identified using the proper orthogonal decomposition analysis.

motion and pitching motion. The periodic components of velocity fluctuations are correlated at all moments of time and these fluctuations are found to contribute significantly to the flow. The qualitative structure of the POD modes identifies the aperiodicity developed in the flow for the periodic oscillations performed by the airfoil.

## FUNDING

The authors like to acknowledge the support provided by the Council of Scientific and Industrial Research (CSIR), Government of India, in the form of Senior Research Fellowship (SRF).

## CONFLICT OF INTEREST

The authors declare that they have no conflicts of interest.

## REFERENCES

1. Oshima, H. and Ramaprian, B., Velocity measurements over a pitching airfoil, *AIAA J*, 1997, vol. 35, no. 1, pp. 119–126.
2. Sarkar, S. and Venkatraman, K., Numerical simulation of thrust generating flow past a pitching airfoil, *Computers Fluids*, 2006, vol. 35, no. 1, pp. 16–42.
3. Deng, J., Sun, L., and Shao, X., Dynamical features of the wake behind a pitching foil, *Phys. Rev. E*, 2015, vol. 92, no. 6, p. 063013.
4. Ashraf, I., Agrawal, A., Khan, M.H., Srivastava, A., Sharma, A., et al., Thrust generation and wake structure for flow across a pitching airfoil at low Reynolds number, *Sadhana*, 2015, vol. 40, no. 8, pp. 2367–2379.
5. Lai, J. and Platzer, M., Jet characteristics of a plunging airfoil, *AIAA J*, 1997, vol. 37, no. 12, pp. 1529–1537.
6. Lewin, G.C. and Haj-Hariri, H., Modeling thrust generation of a two-dimensional heaving airfoil in a viscous flow, *J. Fluid Mech.*, 2003, vol. 492, pp. 339–362.
7. Ashraf, M., Young, J., and Lai, J., Oscillation frequency and amplitude effects on plunging airfoil propulsion and flow periodicity, *AIAA J*, 2012, vol. 50, no. 11, pp. 2308–2324.
8. Martín-Alcántara, A., Fernández-Feria, R., and Sanmiguel-Rojas, E., Vortex flow structures and interactions for the optimum thrust efficiency of a heaving airfoil at different mean angles of attack, *Phys. Fluids*, 2015, vol. 27, no. 7, p. 073602.
9. Guglielmini, L. and Blondeaux, P., Propulsive efficiency of oscillating foils, *Europ. J. Mech-B/Fluids*, 2004, vol. 23, no. 2, p. 255–278.
10. Moriche, M., Flores, O., and Garcia-Villalba, M., On the aerodynamic forces on heaving and pitching airfoils at low Reynolds number, *J. Fluid Mech.*, 2017, vol. 828, pp. 395–423.
11. Floryan, D., Van Buren, T., Rowley, C.W., and Smits, A.J., Scaling the propulsive performance of heaving and pitching foils, *J. Fluid Mech.*, 2017, vol. 822, pp. 386–397.
12. Zheng, H., Xie, F., Zheng, Y., Ji, T., and Zhu, Z., Propulsion performance of a two-dimensional flapping airfoil with wake map and dynamic mode decomposition analysis, *Phys. Rev. E*, 2019, vol. 99, no. 6, p. 063109.
13. Triantafyllou, M., Triantafyllou, G., and Gopalkrishnan, R., Wake mechanics for thrust generation in oscillating foils, *Phys. Fluids A: Fluid Dyn.*, 1991, vol. 3, no. 12, pp. 2835–2837.
14. Jones, K., Dohring, C., and Platzer, M., Experimental and computational investigation of the Knoller–Betz effect, *AIAA J*, 1998, vol. 36, no. 7, pp. 1240–1246.
15. Vandenberghe, N., Zhang, J., and Childress, S., Symmetry breaking leads to forward flapping flight, *J. Fluid Mech.*, 2004, vol. 506, pp. 147–155.
16. Schnipper, T., Andersen, A., and Bohr, T., Vortex wakes of a flapping foil, *J. Fluid Mech.*, 2009, vol. 633, pp. 411–423.
17. Jones, K. and Platzer, M., Numerical computation of flapping-wing propulsion and power extraction . In: *35th Aerospace Sciences Meeting and Exhibit*, 1997, p. 826.
18. Godoy-Diana, R., Aider, J.L., and Wesfreid, J.E., Transitions in the wake of a flapping foil, *Phys. Rev. E*, 2008, vol. 77, no. 1, p. 016308.
19. Badrinath, S., Bose, C., and Sarkar, S., Identifying the route to chaos in the flow past a flapping airfoil, *Europ. J. Mech.-B/Fluids*, 2017, vol. 66, pp. 38–59.
20. Bose, C. and Sarkar, S., Investigating chaotic wake dynamics past a flapping airfoil and the role of vortex interactions behind the chaotic transition, *Phys. Fluids*, 2018, vol. 30, no. 4, p. 047101.
21. Godoy-Diana, R., Marais, C., Aider, J.L., and Wesfreid, J.E., A model for the symmetry breaking of the reverse Bénard–von Kármán vortex street produced by a flapping foil, *J. Fluid Mech.*, 2009, vol. 622, pp. 23–32.
22. Cleaver, D.J., Wang, Z., and Gursul, I., Bifurcating flows of plunging airfoils at high Strouhal numbers, *J. Fluid Mech.*, 2012, vol. 708, pp. 349–376.
23. Medjroubi, W., Stoevesandt, B., and Peinke, J., Wake classification of heaving airfoils using the spectral/hp element method, *J. Comput. Appl. Math.*, 2012, vol. 236, no. 15, pp. 3774–3782.
24. Andersen, A., Bohr, T., Schnipper, T., and Walther, J.H., Wake structure and thrust generation of a flapping foil in two-dimensional flow, *J. Fluid Mech.*, 2017, vol. 812.



25. Mackowski, A. and Williamson, C., Direct measurement of thrust and efficiency of an airfoil undergoing pure pitching, *J. Fluid Mech.*, 2015, vol. 765, pp. 524–543.
26. Anderson, J., Streitlien, K., Barrett, D., and Triantafyllou, M., Oscillating foils of high propulsive efficiency, *J. Fluid Mech.*, 1998, vol. 360, pp. 41–72.
27. Huq, A.A., Sankar, R.A., Lakshmanan, C., Rukesh, C., Kulkarni, D., Subramanya, M., and Rajani, B., Numerical prediction of aerofoil aerodynamics at low Reynolds number for MAV application, NAL PD CF 910.
28. Ferziger, J.H. and Peric, M., *Computational Methods for Fluid Dynamics*, Vol. 3, Springer, 2002.
29. *OpenFOAM, The Open Source CFD Toolbox User Guide* (2017).
30. Zheng, Z.C. and Wei, Z., Study of mechanisms and factors that influence the formation of vortical wake of a heaving airfoil, *Phys. Fluids*, 2012, vol. 24, no. 10, p. 103601.
31. Wei, Z. and Zheng, Z.C., Mechanisms of deflection angle change in the near and far vortex wakes behind a heaving airfoil. In: *51st AIAA Aerospace Sciences Meeting Including the New Horizons Forum and Aerospace Exposition*, 2013, p. 840.
32. Koochesfahani, M.M., Vortical patterns in the wake of an oscillating airfoil, *AIAA J.*, 1989, vol. 27, no. 9, pp. 1200–1205.
33. Van Buren, T., Floryan, D., and Smits, A.J., Scaling and performance of simultaneously heaving and pitching foils, *AIAA J.*, 2019, vol. 57, no. 9, pp. 3666–3677.
34. Bose, C., Gupta, S., and Sarkar, S., Dynamic interlinking between near- and far-field wakes behind a pitching–heaving airfoil, *J. Fluid Mech.*, 2021, vol. 911, p. A31.
35. Vineeth, V.K., Patel, D.K., Roy, S., Goli, S., and Roy, A., Investigations into transient wakes behind a custom airfoil undergoing pitching motion, *Europ. J. Mech.-B/Fluids*, 2019, vol. 85, pp. 193–213.
36. Ohmi, K., Coutanceau, M., Loc, T.P., and Dulieu, A., Vortex formation around an oscillating and translating airfoil at large incidences, *J. Fluid Mech.*, 1990, vol. 211, pp. 37–60.
37. Heathcote, S. and Gursul, I., Jet switching phenomenon for a periodically plunging airfoil, *Phys. Fluids*, 2007, vol. 19, no. 2, p. 027104.
38. Williamson, C.H. and Roshko, A., Vortex formation in the wake of an oscillating cylinder, *J. Fluids Struct.*, 1988, vol. 2, no. 4, pp. 355–381.
39. Dynnikova, G.Y., Dynnikov, Y.A., and Guvernyuk, S., Mechanism underlying Kármán vortex street breakdown preceding secondary vortex street formation, *Phys. Fluids*, 2016, vol. 28, no. 5, p. 054101.
40. Dynnikova, G.Y., Dynnikov, Y.A., Guvernyuk, S., and Malakhova, T., Stability of a reverse Kármán vortex street, *Phys. Fluids*, 2021, vol. 33, no. 2, p. 024102.
41. Saha, A.K., Muralidhar, K., and Biswas, G., Vortex structures and kinetic energy budget in two dimensional flow past a square cylinder, *Computers Fluids*, 2000, vol. 29, no. 6, pp. 669–694.
42. Sirovich, L., Turbulence and the dynamics of coherent structures. I. Coherent structures, *Quart. Appl. Math.*, 1987, vol. 45, no. 3, pp. 561–571.
43. Vineeth, V.K. and Patel, D.K., Propulsion performance and wake transitions of a customized heaving airfoil, *Intern. J. Modern Phys. C*, 2021, vol. 32, no. 9, pp. 1–28.